



Universidad  
Carlos III de Madrid  
[www.uc3m.es](http://www.uc3m.es)

Nils Dennis Nothnagel

**Development of novel quantitative medical imaging  
techniques for MPI and MRI**



Universidad  
Carlos III de Madrid  
www.uc3m.es

# ***TESIS DOCTORAL***

## ***Development of novel quantitative medical imaging techniques for MPI and MRI***

**Autor:**

***Nils Dennis Nothnagel***

**Directores:**

**Javier Sánchez-González**

**Borja Ibáñez**

**Tutor:**

**Manuel Desco Menéndez**

**DEPARTAMENTO DE BIOINGENERÍA E INGENIERÍA AEROESPACIAL**

Leganés, septiembre 2016





Universidad  
Carlos III de Madrid  
www.uc3m.es

## THESIS DOCTORAL

### Development of novel quantitative medical imaging methods for MPI and MRI

**Autor:** *Nils Dennis Nothnagel*

**Directores:**

**Javier Sánchez-González**

**Borja Ibáñez**

**Tutor:**

**Manuel Desco Menéndez**

Firma del Tribunal Calificador:

Firma

Presidente:

Vocal:

Secretario:

Calificación:

Leganés, septiembre de 2016

# Table of Content

<b>Abstract .....</b>	<b>i</b>
<b>Resumen.....</b>	<b>iii</b>
<b>List of Abbreviations .....</b>	<b>v</b>
<b>1. Medical Imaging with MPI and MRI .....</b>	<b>1</b>
1.1 Magnetic Particle Imaging .....	1
1.2 Cardiac imaging techniques for Magnetic Resonance Imaging .....	5
<b>2. Motivation and Objectives of the Thesis .....</b>	<b>15</b>
2.1 Motivation .....	15
2.2 Objectives .....	16
2.3 Outline of the document .....	18
<b>3. Measurement of System Function with extended Field-of-View .....</b>	<b>19</b>
3.1 Introduction .....	19
3.2 Material and Methods .....	20
3.3 Results.....	25
3.4 Discussion and Conclusion .....	26
<b>4. VF 3D-BRISA: Very Fast 3D BReath-hold Isotropic imaging using Spatio-temporal Acceleration for non-angulated whole-chest 3D cardiac cine MRI .....</b>	<b>29</b>
4.1 Introduction .....	29
4.2 Theory.....	30
4.3 Methods.....	34
4.4 Results.....	36
4.5 Discussion .....	42
4.6 Conclusion.....	44
<b>5. In-vivo validation of non-angulated whole-heart cardiac cine imaging using VF 3D-BRISA.....</b>	<b>45</b>
5.1 Introduction .....	45
5.2 Material and Methods .....	46
5.3 Results.....	48
5.4 Discussion .....	52
5.5 Conclusion.....	54
<b>6. Discussion and Conclusion .....</b>	<b>55</b>
7.1 Future lines of research starting from the thesis.....	58
<b>7. Publications .....</b>	<b>61</b>
<b>8. Bibliography.....</b>	<b>63</b>







## Abstract

Tomographic imaging has become indispensable in the clinical routine. In a tomographic scan, images of the inner human body are produced without the need of dissecting the human skin. The common types of medical images are two-dimensional slices and entire three-dimensional volumes. To image dynamic processes such as organ function or perfusion, time series are produced at multiple spatial locations. To date, the most common medical imaging modalities are X-ray imaging, Computed Tomography (CT), Magnetic Resonance Imaging (MRI) or tracer-based imaging such as Positron-Emission Tomography (PET) or Single-Photon Emission Tomography (SPECT). Next to the common modalities, a novel medical imaging modality called Magnetic Particle Imaging (MPI) has been introduced, and its position between the established modalities still needs to be defined.

In general, cardiovascular applications impose specific challenges on medical imaging. Imaging speed is required to compensate for respiratory and cardiac motions, and to capture rapid uptake rates of contrast agents in the heart tissue. At the same time, high spatial resolution is demanded to accurately assess cardiac anatomy. In this work, we focus on two main cardiovascular applications: cardiac perfusion imaging and cardiac function imaging.

Each imaging modality stands out with particular advantages and drawbacks for cardiovascular imaging. Magnetic Resonance Imaging (MRI), for example, has its main advantage in the use of non-ionizing radiation and its superb soft-tissue contrast and is hence suitable for cardiac function assessment. However, due to non-linearity of the MR signal with the contrast concentration, an application such as cardiac perfusion imaging is challenging and requires complex mathematical and practical treatment to measure the arterial input function. A more adequate tool for application on perfusion imaging would be Magnetic Particle Imaging (MPI) since its signal is linear with the contrast concentration over a wide range of concentration. Yet, a drawback of MPI is that no anatomic information is inside the MPI images since it is a purely tracer-based imaging method such as PET or SPECT. Therefore, image registration is required to fuse anatomic reference scans with MRI or CT with obtained MPI images in order to locate cardiac tissues.

Magnetic Particle Imaging (MPI) renders for the application on cardiac perfusion imaging, due to its high spatial and temporal resolution and the linearity of the signal with the contrast concentration. Nevertheless, spatial coverage of MPI is currently limited to small volumes, thus there is a need for extended spatial coverage to assess human tissue structures maintaining high

temporal resolution. In this work, methods are explored to extend spatial coverage with the aim to improve image registration of MPI images with anatomic reference scans from MRI or CT.

Magnetic Resonance Imaging (MRI) is a suitable tool for cardiac function assessment. Cardiac cine imaging is the standard method to acquire heart motion during the entire cardiac cycle. Though, practical challenges still remain in the clinical application of cardiac cine MRI. The common way to obtain cine images is a stack of slices in short axis and long axis orientation, each acquired during 10-12 separate breath-holds. This is a time-consuming task and can be a tedious procedure especially for elder or ill patients in a clinical scenario. Additionally, due to possible patient movements between the breath-holds, slices at different locations can be miss-aligned leading to decreased accuracy in the assessment of cardiac function.

We introduce and implement in this work a novel method for cardiac cine MRI called VF 3D-BRISA (“Very Fast 3D Breath-hold ISotropic Imaging using Spatio-temporal Acceleration”) allowing high image acceleration rates of over 30 and implement it on a real 3T MRI system. The high image acceleration is appreciated to perform non-angulated isotropic 3D cine imaging in a single breath-hold, overcoming the challenges of multi-slice 2D cine imaging.

For the objective of this thesis, 2D and 3D experiments are conducted to assess optimal imaging parameters for VF 3D-BRISA. Furthermore, we conduct an in-vivo validation study of VF 3D-BRISA to demonstrate that cardiac function can be assessed with the same accuracy as with a reference method of 2D multi-slice cine imaging.

## Resumen

Obtener imágenes mediante equipos de tomografía se ha convertido en una parte indispensable en la rutina clínica. Durante una examinación tomográfica, se producen imágenes del interior del cuerpo humano sin la necesidad de disectar la piel humana. La forma más común es a través de cortes bidimensionales o volúmenes tridimensionales completos. Para capturar procesos dinámicos tales como la función o la perfusión de un órgano, se adquieren en diferentes momentos y ubicaciones espaciales. Las técnicas de imagen más comunes son típicas de imágenes de rayos X, tomografía computarizada (TAC), resonancia magnética (RM) o de imágenes basadas en trazador: como Tomografía por Emisión de Positrones (PET) o tomografía por emisión de fotón único (SPECT). Paralelo a las modalidades comunes, se ha introducido una técnica nueva llamada Imaging de Partículas Magnéticas (MPI) y su posición entre las modalidades establecidas todavía está por definirse.

En general, se imponen retos específicos sobre una aplicación cardiovascular de equipos tomográficos. Se requiere velocidad de adquisición para compensar los movimientos respiratorios y cardíacos, y para capturar bien las tasas de absorción rápida de agentes de contraste en el tejido cardíaco. Al mismo tiempo, se exige una alta resolución espacial para evaluar con más precisión la función cardíaca. En esta tesis, nos centramos en las dos principales aplicaciones cardiovasculares: La imagen de perfusión cardíaca y la imagen de función cardíaca.

Cada modalidad de tomografía se destaca con sus ventajas e inconvenientes particulares para aplicaciones cardiovasculares. Imagen por Resonancia Magnética (RM), por ejemplo, tiene su principal ventaja en el uso de las radiaciones no ionizantes y su excelente contraste de los tejidos blandos y, por tanto, es adecuada para la evaluación de la función cardíaca. Sin embargo, debido a la no-linealidad de la señal de RM con la concentración de contraste, obtener imágenes de perfusión cardíaca con la RM es difícil y requiere tratamiento matemático y un manejo complejo para medir la función de entrada arterial (“arterial input function”, AIF). Una herramienta más adecuada para la aplicación en imágenes de perfusión es Imaging de partículas magnéticas (MPI), ya que su señal es lineal con la concentración de contraste en un amplio intervalo de concentración. Sin embargo, un inconveniente de MPI es que no hay información anatómica dentro de las imágenes MPI ya que es un método de formación de imágenes basado a trazadores tal como PET o SPECT, por lo que requiere exploraciones de referencia anatómicas con RM o TAC para la fusión de imágenes con imágenes MPI para localizar la ubicación de tejido cardíaco.

Imaging de Partículas Magnéticas (MPI) puede ser adecuada para la aplicación de imágenes de perfusión cardíaca, debido a su alta resolución espacial y temporal y la linealidad de la señal con la concentración de contraste. No obstante, la cobertura espacial de MPI se limita actualmente a pequeños volúmenes, por lo tanto se desea una necesidad de cobertura espacial extendida para evaluar las estructuras de tejido humano. En esta tesis, se trabajan métodos para ampliar la cobertura espacial manteniendo alta resolución temporal. Se estima que una cobertura espacial más amplia mejora el registro de imágenes, de imágenes MPI con imágenes de referencia anatómicas por resonancia magnética o tomografía computarizada.

La Resonancia Magnética (RM) es adecuada para la evaluación de la función cardíaca. Es el método estándar para adquirir el latido del ventrículo izquierdo durante todo el ciclo cardíaco a través de las imágenes “cine” cardíaca. Aunque, prevalecen desafíos prácticos aún en la aplicación clínica de MRI cine cardíaco. La forma más común de obtener imágenes de cine cardíacas es a través de un grupo de cortes de orientación en eje corto y eje largo, cada uno adquirido en 10-12 apneas separadas. Esta tarea consume tiempo y puede ser un procedimiento tedioso, especialmente para pacientes ancianos y/o enfermos en un escenario clínico. Además, debido a posibles movimientos del paciente entre la retención de respiración, sectores en diferentes lugares pueden ser mal alineados reduciendo la exactitud en la evaluación de la función cardíaca.

En esta tesis, se introduce un nuevo método para resonancia magnética cardíaca llamada VF-3D BRISA ("Very Fast 3D Breath-hold ISotropic Imaging using Spatio-temporal Acceleration") que permite grados altos de aceleración de cine RM cardíaca. Se implementa BRISA en un sistema de RM 3T. Se aprecia esta aceleración alta para adquirir imágenes cine 3D isótropo completo en una sola apnea, superando los retos de la adquisición en múltiples cortes 2D en el estándar cine durante múltiples apneas.

Se llevan a cabo experimentos en 2D y 3D para evaluar los parámetros óptimos para la formación de imágenes en 3D VF-BRISA. Además, se lleva a cabo un estudio de validación in vivo de la 3D-VF-BRISA para demostrar que la función cardíaca puede evaluarse con la misma precisión que con el método de referencia utilizando el estándar 2D cine de cortes múltiples.

## List of Abbreviations

<b>AP</b>	Anterior-Posterior (Orientation)
<b>CMR</b>	Cardiac Magnetic Resonance Imaging
<b>CS</b>	Compressed Sensing
<b>CT</b>	Computed Tomography
<b>ECG</b>	Electrocardiogram
<b>FH</b>	Foot-Head (Orientation)
<b>FFE</b>	Fast Field Echo ( MR Sequence )
<b>FFL</b>	Field-Free Line
<b>FFP</b>	Field-Free Point
<b>FOV</b>	Field of View
<b>LV EDV</b>	Left-Ventricular End-Diastolic Volume
<b>LV EF</b>	Left-Ventricular Ejection Fraction
<b>LV ESV</b>	Left-Ventricular End-Systolic Volume
<b>MPI</b>	Magnetic Particle Imaging
<b>MRI</b>	Magnetic Resonance Imaging
<b>RL</b>	Right-Left (Orientation)
<b>SENSE</b>	Sensitivity Encoding
<b>TR</b>	Repetition time
<b>TE</b>	Echo time



# 1. Medical Imaging with MPI and MRI

## 1.1 Magnetic Particle Imaging

Magnetic Particle Imaging (MPI) is a novel medical imaging technology that has been invented by Philips Research Laboratories, Hamburg, in 2001 by Bernhard Gleich und Jürgen Weizenecker and has been published first in “Nature” in 2006 (1). MPI is a method that visualizes the concentration of an applied contrast agent, similar to Position-Emission Tomography (PET) or Single-Photon Emission Computed Tomography (SPECT) without ionizing radiation. Briefly after its first technical publication, a preclinical demonstrator system has been built and applied on cardiac in-vivo imaging of a mouse model with 3D-encoded volumes at a frame rate of 46 volumes per second(2). The signal in MPI is generated by a fluid of super-paramagnetic iron oxide particles (“SPIO”) that are interacting with an oscillating magnetic field, in MPI called “Drive Field”. The characteristic of the SPIOs is that its magnetization curve can be approximated by a Langevin curve which is highly non-linear and without hysteresis. Based on Faradays law, time-changing magnetization induces a current in a receive coil which can be separated from the feed-through interference of the excitation frequency by a band-stop filter. A sound introduction to MPI and signal generation can be found in(3).

Briefly, the design of an MPI scanner is usually based on hardware components that generate and move a “Field-Free Point” (FFP) or a “Field-Free-Line” (FFL). The movement of the FFP over the SPIOs stimulates a time changing magnetization and thus a voltage signal in the receive coils. The main field in MPI is conventionally named “Selection Field” as it generates or selects the region of the FFP or FFL. It can be created by two opposing magnets in Maxwell configuration or by an open coil design applying all magnetic fields from one side (4)(5). As long as the particles are outside the FFP or the FFL region, their magnetization is saturated and aligns with the local magnetic field of their surrounding area and thus generates no signal. Eventually, when the FFP is moved over the position of an SPIO, its magnetization follows the local magnetic field instantly and hence induces a signal peak in the receive coils. On Fig. 1, the principle of signal excitation for MPI is visualized. It consists of an oscillating field strength  $H(t)$  with a pure sinusoidal frequency in kHz-range and a small field amplitude of several  $\text{mT}/\mu_0$ . This field, conventionally named “Drive Field”, superimposes the Selection Field to drive the FFP on a fast movement with small amplitude. The resulting magnetization curve  $M(H(t))$  is transformed into a signal which spectrum contains higher harmonics of the

excitation frequency. After signal recording, the signal from the SPIOs can be separated from the feed-through interference of the Drive Field by a band-stop filter. The remaining signal spectra from the higher harmonics contain thus pure MPI signals from the particles and give direct quantitative information about the particle concentration. In MPI, up to the 40<sup>th</sup> harmonics can be detected. To compare MPI with MRI, the reason why MPI is fast is because all frequencies of the k-space are measured simultaneously (see k-space definition in the Chapter 1.2). Conventional MRI, in contrast to MPI, is a technique that measures frequencies one-by-one in conventional Cartesian k-space or with few frequencies simultaneously at a time by advanced k-space sampling trajectories such as spiral or radial sampling.

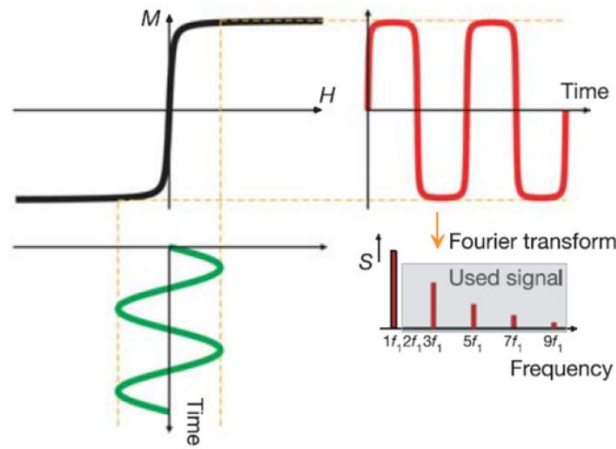


Figure 1. Basic signal generation in MPI (1). A sinusoidal excitation field  $H(t)$  (green curve) is transformed into a magnetization curve  $M(H(t)t)$  (red curve) via the non-linear Langevin model of the particle magnetization response (black curve). After Fourier transform, signal processing is applied to suppress the excitation frequency  $f_1$  of the recorded signal. The higher harmonics  $3f_1, 5f_1, 7f_1$  are used for image reconstruction.

Mathematically, the image reconstruction follows a linear model that can be described as suggested by Knopp (6). In this approach, the signal generation is described as a linear system model that transforms a particle concentration in the spatial domain to a measured signal. The image reconstruction consists then as inversion of the system model. With an infinitesimal spectral signal response  $u_i$  of a particle concentration  $c$  in a spatial region  $\Omega$  at a spatial position  $r \in \Omega$ , one can write the measured frequency component  $\hat{f}_i$  by

$$\hat{f}_i = \int_{r \in \Omega} u_i(\vec{r})c(\vec{r})d\vec{r} \quad (1)$$

In a discretized version, assuming point-like signal sources in a FOV with  $N$  voxel containing particle concentration  $c_i$ , and the spectral response  $u_i$  of a point-like sample from voxel  $i$ , equation (1) is transitioned to

$$\hat{f}_i = \sum_{i=0}^N u_i(\vec{r}) c_i(\vec{r}) \quad (2)$$

Taking into account all measured frequency components  $\vec{f}$  of the MPI scan, equation (2) can be written in matrix notation with a linear system matrix  $U$  and the particle concentration  $\vec{c}$  as

$$\vec{f} = U \vec{c} \quad (3)$$

Then, the image reconstruction of the particle concentration  $\vec{c}$  can be written as the matrix inversion of equation (3) by

$$\|U \vec{c} - \vec{f}\|^2 = \min! \quad (4)$$

This linear system of equation can be solved by a Conjugate Gradient algorithm, for instance, or by a Kaczmarz method(7). Additionally, to increase SNR a regularization term with a regularization weight  $\lambda$  can be introduced in equation (4) to

$$\|U \vec{c} - \vec{f}\|^2 + \lambda \|\vec{c}\|^2 = \min! \quad (5)$$

However at the cost of decreased spatial resolution. A more in-depth description of the image reconstruction process and the structure and acquisition of the system matrix  $U$  can be found in (8).

The Field-of-View in basic MPI is limited to a small region due to physiological limits. As the Drive Field operates in the kHz range, its amplitude needs to be limited in order to avoid nerve stimulation and is typically in the range of below  $20 \text{ mT}/\mu_0$  (9). In general, a Drive Field-only encoded FOV is limited by the Drive Field Amplitude  $H$  and the field gradient strength  $G$

$$FOV = 2 H / G, \quad (6)$$

in a MPI system where the FFP is generated by a linear field gradient  $G$ . Hence, the movement of the FFP and thus the range in which signal can be generated is limited by only a volume of few cubic centimeters, see figure 2a. For example, in an MPI system with a linear field gradient of  $G=1.25 \text{ T/m}/\mu_0$  and a Drive field amplitude of  $15 \text{ mT}/\mu_0$ , the basic FOV is limited to 24.0 mm. To extend the FOV, a concept has been introduced that uses low-frequency offset fields that can operate at larger field amplitudes(10). The method is visualized on Figure 2b and is conventionally named ‘‘Multi-Station MPI’’. The principle is to shift the complete FFP encoded region of the Drive Field by static offset fields, the so-called Focus Fields, on several neighboring stations, see Figure 2b. Thus, a larger region can be encoded at the cost of temporal resolution as every station needs to be acquired successively. Additionally, some extra time is

needed to switch from one station to the next. With this strategy, multi-station MPI has been realized using 12 Focus field stations enlarging the FOV to a region of  $34.5 \times 24.3 \times 17.0 \text{ mm}^3$ , however at a reduced repetition time of 517 milliseconds per volume (11). This approach has drawbacks for dynamic acquisition since to each small volume will have slightly different information from another.

To make use of the MPI signal also during the switching time, the temporal resolution can be increased or SNR can be gained. A method to reconstruct MPI signals acquired during the transition between focus field stations is visualized on Fig. 2c. Here, MPI signal is recorded on the linear transition and reconstructed with a modified system function(12). In this work, the transition speed of the Focus Field was smaller than one encoded voxel per Drive Field repetition time. In a following work, the maximum speed limit of the linear FOV transition was increased to a speed limit of several voxels per Drive field repetition time (13).

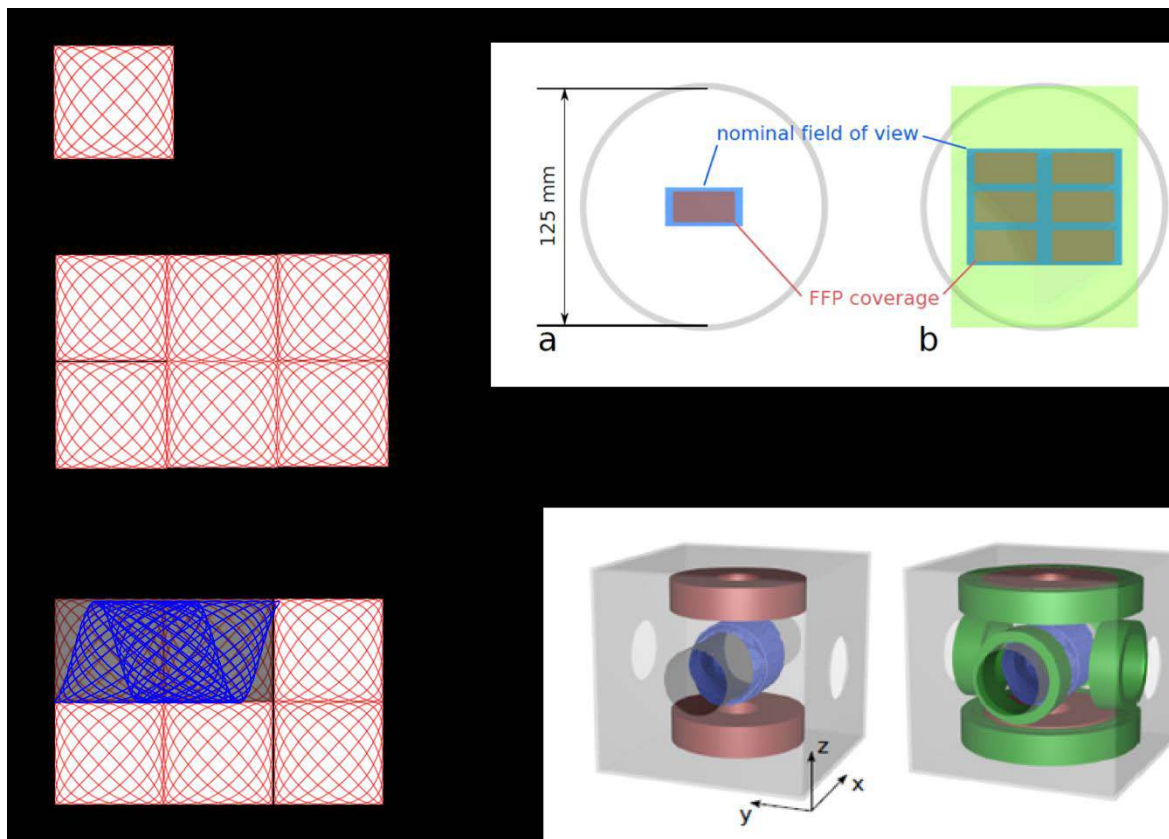


Figure 2. (a) basic small FOV of MPI , encoding only by Drive Fields (b) multi-station MPI making use of static offset fields or so-called “Focus Field” to shift the entire small imaging volume (c) multi-station MPI imaging recovering MPI signal during the transition from one focus field station to another (d) FOV positions in the scanner bore or an MPI system taken from (14) (e) sketch of the additional hardware to superimpose the Drive Fields with the Focus Field system based on electromagnets generating static magnetic offset fields .

The idea presented in this work is to evaluate the performance of MPI during transitions of more complex movements of the FOV and not only on during linear movements. Also, continuously moving FOV trajectories are investigated instead of waiting periods on Focus Field stations. The goal was to prepare fast cardiac MPI sequences that require both high temporal resolution in order to capture the contrast dynamics of cardiac perfusion and large spatial coverage to facilitate image registration to anatomic reference pre-scans. The performance of the modified system function from (15) is compared with an approach to measure an extended system function containing the whole encoded region of Drive Fields and Focus Fields combined with an appropriate regularization.

## 1.2 Cardiac imaging techniques for Magnetic Resonance Imaging

Magnetic Resonance Imaging (MRI) has become a gold-standard for many non-invasive medical imaging applications due to its superb soft-tissue contrast and its use of non-ionizing magnetic fields. The basic phenomenon of MRI, the spin resonance, has been discovered in 1946 by Bloch and Purcell. It is based on the property of certain atoms such as  $^1\text{H}$  or  $^{13}\text{C}$  to have a magnetic moment or spin that rotates around its axis with a precession frequency that depends on the surrounding magnetic field. In a resonance excitation of those atoms, the spins are twisted out of their normal rotation movement by radiofrequency pulses. Based on the relaxation times, also called  $T_1$  and  $T_2$  relaxation times, much useful clinical information can be gained about the function and the local structure of tissue. In 1971, Mansfield and Lauterbur were the first who applied the spin resonance phenomenon on medical imaging and gained the first tomographic MRI image of a human body(16,17).

Since its invention in the seventies, MRI has gone through decades of hardware and software development. To-date MRI scanners have reached a speed that enables clinical application on dynamic processes like cardiovascular imaging. On figure 3 is shown a picture of a state-of-the-art MRI scanner and on figure 3b a sketch of its main hardware components. The first component of a conventional MRI scanner is a superconductive coil element. It generates a homogeneous  $B_0$ -field with high field homogeneity of around 10 ppm over a large area inside the bore. The purpose of the main field is to align the rotation of the  $^1\text{H}$  spins along the main axis of the magnetic field. The second main hardware component is the gradient system that superimposes the main magnetic field with linear field gradients. It consists of three independent systems for x,y and z that generate each orthogonal gradient fields of the z-component and is used for spatial encoding of the MR signal. The third component is the radio-frequency (RF) system that is used to excite the rotating  $^1\text{H}$ -spins at their characteristic

resonance frequency, the so-called Larmor frequency. The Larmor frequency  $\omega_L$  is related to the local magnetic field strength  $B$  and is given by

$$\omega_L = \gamma B, \quad (7)$$

with the gyromagnetic constant  $\gamma$ , which is characteristic for each nucleus. For instance,  $^1\text{H}$  has a gyromagnetic constant of  $\gamma_H = 42.58 \text{ MHz/T}$ . Usually, the RF system is tuned to the frequency range of  $^1\text{H}$  as the human body is around 70 % made of water ( $\text{H}_2\text{O}$ ) molecules. It consists of an excitation and receive system that stimulates and records the generated MR signal and is placed on the subject as a surface coil.



Figure 3: (a) State-of-the-art MRI scanner (b) sketch of the main MRI hardware components taken from (18): main magnet, linear field gradient, RF system

The conventional way to acquire an MRI image is the so-called Fourier imaging mode. Briefly, the recorded MRI time-domain signal  $S(t)$  for magnetic moments of a  $^1\text{H}$  density distribution  $\rho(x)$  depends on the local magnetic field  $B = B_0 + Gx$ . The magnetic field  $B$  consists of a superimposition of the main magnetic field  $B_0$  and the linear field gradient, leading to a Larmor frequency  $\omega = \gamma (B_0 + Gx)$  (eq. 7) and a recorded MRI signal

$$S(t) = \int_{-\infty}^{\infty} \rho(x) e^{-i\omega t} dx \quad (8)$$

for an MRI experiment in one spatial dimension. Defining the value

$$k(t) = \int_0^t \gamma G(t) dt, \quad (9)$$

the MRI signal of eq.8 can hence be written in a so-called “k-space” formulation of MRI Fourier imaging as

$$S(k) = \int_{-\infty}^{\infty} \rho(x) e^{-i2\pi kx} dx \quad (10)$$

which is in the form of the conventional well-known Fourier transform in one dimension. After discretization, it follows that

$$S(k_j) = \sum_{i=0}^N \rho(x_i) e^{-i2\pi k_j x} \quad (11)$$

In this case, image reconstruction can be performed via the mathematical application of the inverse Fourier transform when all frequencies  $S(k_j)$  of an MRI spectrum are measured. A more detailed description can be found in(19).

As a consequence of the inverse Fourier relationship, the FOV in MRI imaging is determined by the k-space sampling rate  $\Delta k$  . In the same manner, the resolution  $\Delta x$  of the MRI image is determined by the maximum k-space value  $k_{max}$  by

$$\begin{aligned} \text{FOV} &= \frac{1}{2 \cdot \Delta k} \\ \Delta x &= \frac{1}{2 \cdot k_{max}} \end{aligned} \quad (12)$$

The fundamental connection between the final image and its measurement in the Fourier domain is visualized on Figure 5. The image and its k-space representation is linked via Fourier transform. Many developments have been achieved for fast sampling strategies of the k-space; such as spiral or radial trajectories, or recent research includes random under-sampling with variable density sampling (20–23). However, Non-Cartesian sampling of the k-space requires other reconstruction techniques than Fourier transform such as NUFFT or Compressed Sensing Reconstruction(24,25).

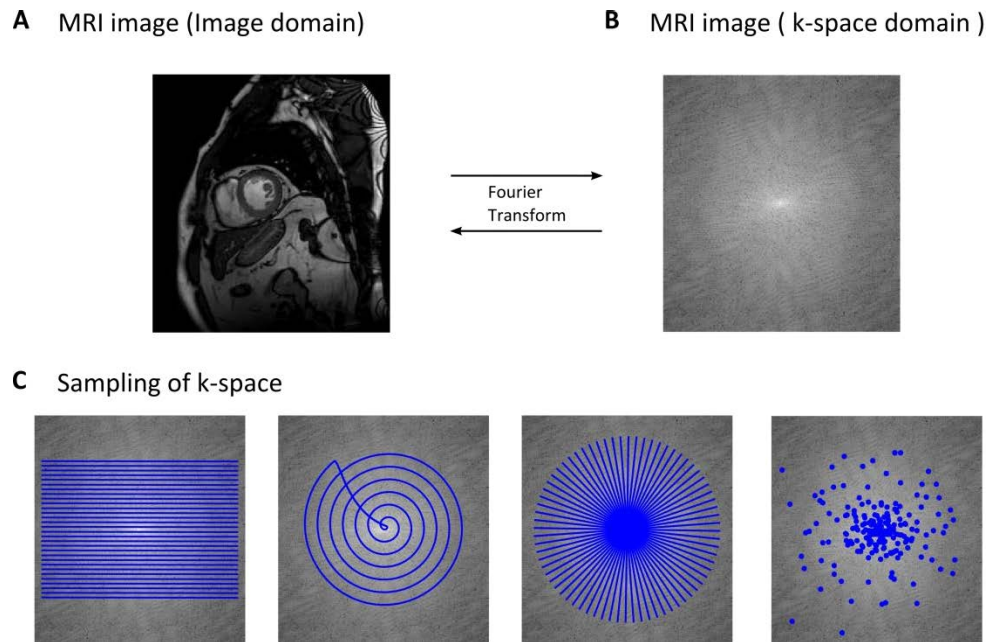


Figure 5: (a) short axis MRI image of a human heart (b) k-space or frequency representation of the same MRI image. The two images are linked via Fourier transform. (c) MRI sampling strategies of the k-space via different trajectories : Cartesian, Spiral, Radial, Random sampling with Variable density distribution .

At this point, it becomes clear that MRI is in principle a slow imaging method. Physiological limits for nerve stimulation of the gradient switching in eq. 9 ultimately limit the hardware acceleration of Fourier imaging as only one k-space profile at a time can be measured. The time between two k-space profiles, also characterized by the “slew rate” of the MRI system, is determined by the maximum gradient strength and limited by general public exposure limits of electromagnetic fields(26).

However, many techniques have been developed to accelerate MRI imaging by an incomplete sampling of k-space. The key concept is to omit k-space samples and recover the missing frequencies by an additional reconstruction next to the inverse Fourier transform. Many methods have been proposed in the recent years, such as

- Partial Fourier imaging (27)
- Parallel imaging (28–30)
- Compressed sensing (31,32)
- Simultaneous multi-slice excitation (SMS) (33)

After further improvements of MRI imaging hardware in the recent years and the development of image acceleration techniques, MRI has ultimately emerged as a clinical tool for

cardiovascular imaging. A cardiovascular MRI scan to measure the cardiac function usually consists of the assessment of the left-ventricle function. The ventricle is segmented into 15-17 slices in short-axis orientation as indicated on Figure 5a. Clinically relevant time-information of the muscle contraction can be acquired in a so-called “cine” mode that generates movie-like images of the heart. The entire cardiac cycle is segmented from the detection of the RR wave over systole to diastole into small windows of typically 20-60 milliseconds. For each small time frame, a full image is acquired. Two exemplary time frames of the cardiac cycle are shown on Fig. 5b, showing the contraction of the dark muscle tissue and the bright blood pool. The small time windows are conventionally named as “time stamps” or “cardiac phases”, and typically 15-30 phases are acquired for each slice. Therefore, a total number of 200-500 images are acquired per cine scan taking into account all slices and all cardiac phases. More details can be found in (34).

Due to chest movement during breathing, cardiac imaging typically requires breath-hold acquisitions, with a scan of typically one or two slices per breath-hold. To synchronize the MRI acquisition with the heartbeat, the patient is equipped with a non-magnetic ECG trigger or a pulse oximetry device to detect the RR waves of the cardiac cycle. From a k-space point of view, in every cardiac phase a full k-space needs to be acquired, as depicted on Fig. 5c. As the acquisition of all k-space profiles typically takes longer than the duration of one cardiac phase, the acquisition is segmented into small parts of the k-space. Then, the k-space is acquired segment-by-segment in every RR interval until the end of the breath-hold which is typically between 10 to 20 seconds. The procedure is repeated in successive breath-holds until all short axis slices of the ventricle are acquired, which can be a tedious procedure for the examined patient especially in a clinical scenario.

The cardiac cine MRI post-processing is visualized on Fig. 6. For cardiac function analysis, the stack of acquired short-axis slices is loaded in a cardiac MRI analysis workstation. From the data, the goal is to obtain quantitative clinical data such as systolic and diastolic left-ventricle volume, left-ventricle mass, stroke volume or ejection fraction. The main step in cardiac analysis consists of manual or semi-automatic segmentation of the left-ventricle contours between blood and muscle tissue. The segmentation process needs to be done for each slice and each cardiac phase and can be a tedious procedure. After segmentation, the volumetric measurements are obtained by numerical integration of the 2D contours, for instance via Simson rule (35).

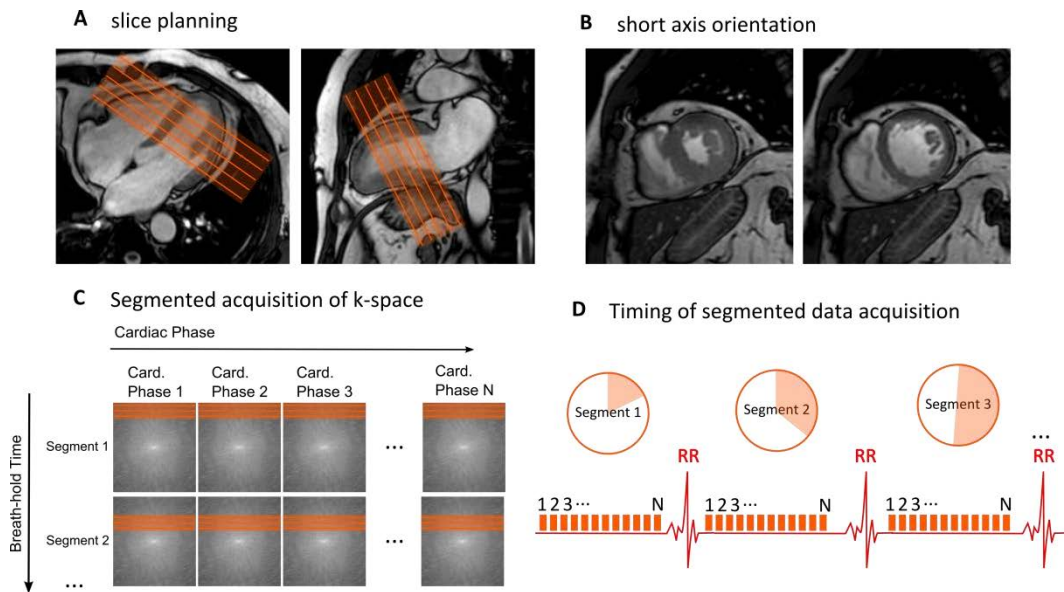


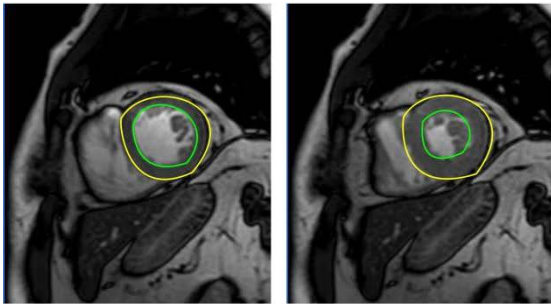
Figure 5: (a) slice planning of short axis orientation of the left-ventricle (b) two time frames or cardiac phases of the cardiac cycle, showing the contraction of the ventricle (c) MRI sampling strategies of the k-space for a cardiovascular cine acquisition. The k-space is acquired segment-by-segment in every RR interval, synchronized with the heart beat by an ECG trigger or by pulse-oximetry. During one RR interval, all cardiac phases of a k-space segment are acquired (b) After sufficient RR intervals during the breath-hold, all segments with all cardiac phases are acquired.

At this point, it becomes obvious why cardiovascular applications of MRI are a challenging task and why image acceleration plays an essential role in this specific field. Ultimately, the duration of the breath-hold determines the spatial and temporal resolution. Hence, image acceleration techniques can help to improve spatial or temporal resolution maintaining the same scan time. Alternatively, it can enable to acquire cardiac slices in the same resolution at a shorter time, for example with two or more slices during one breath-hold.

In addition to the previously mentioned general acceleration techniques, many dedicated MRI cine techniques have been developed for the acceleration of cardiovascular imaging. Famous techniques of cardiac cine acceleration techniques are:

- View Sharing (36)
- Keyhole Imaging (37)
- K-t kernel based methods (38)
- Reduced Field-of-View techniques for cardiac cine MRI (39)
- Cardiac Compressed Sensing (40,41)

A Contour segmentation



B stack of segmented short axis

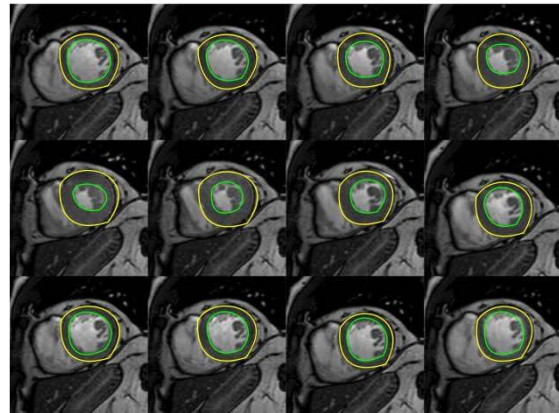


Figure 6. Contour drawing of cine images, two example time frames (b) stack of segmented short axis images from cine scan. From this data, quantitative volumetric data such as systolic and diastolic volumes and left-ventricle mass can be obtained by numerical integration of the segmented short axis images, for example via Simpson rule.

The first main acceleration technique applied on cardiac cine imaging is parallel imaging. From a k-space perspective, parallel imaging is the possibility to acquire multiple k-space profiles at the same time. The level of simultaneous k-space profile acquisition depends on the applied reconstruction method, the geometry of the sensitivity for the receiving system and the required SNR. Image acceleration obtained by parallel imaging lies typically in the range between two and eight.

In general, parallel imaging is based on recording the MRI signal simultaneously on different receive channels. The receive coils are designed in a way that every channel has a different location and a rather unique and inhomogeneous spatial sensitivity profile. Hence, the images have a unique pattern on every channel as they are modulated with the coil sensitivity. The inhomogeneity of the received signal is exploited to introduce an additional spatial encoding effect complementary to conventional Fourier imaging. Thus, with the additional information of the multiple receive channels it becomes possible to unfold the information of the simultaneously acquired k-space profiles. A detailed introduction can be found in (42).

Another large group of cardiac MRI acceleration techniques are reduced-Field-of-View methods. From a k-space point of view, reducing the FOV is increasing the spacing between k-space samples. Thus, the area covered by the highest k-space samples (which defines the spatial resolution) can be sampled in a shorter time due to lower required sampling rates. However, since large parts of the imaged FOV usually contains static tissue regions during cine imaging,

the corresponding cardiac MR signal of the static tissue is rather constant over time, which introduces a spatio-temporal redundancy in the acquired data and can thus be appreciated in several acceleration methods. Examples for reduced FOV techniques are:

- UNFOLD (39)
- kt-BLAST or kt-SENSE (38)
- NoQuist (43)
- PINOT (44)
- ZOOM imaging (45)

A third group of cardiac MRI acceleration methods are based on Compressed Sensing or sparse reconstruction. Sparse matrices contain only zeros except very few non-zero elements. The idea of sparse reconstruction is that MRI images are compressible to a sparse representation and already few random k-space samples are sufficient information for an approximate image reconstruction. The reconstruction process is performed with a non-linear procedure in a sparse domain. As the number of k-space samples is small, acquisition time is significantly reduced. A sparse transform for the MRI images can be the Fourier transform, but also Finite Difference or Wavelet transforms are investigated to treat the reconstruction as denoising problem which is well established in wavelet theory. Recent research shows the successful application of Compressed Sensing on preclinical and clinical cardiac cine MRI (41,46). However, Compressed Sensing strategies are still only used inside the research community and many obstacles need to be overcome to incorporate the methods in a clinical environment. One of such obstacles is the long reconstruction time needed for the non-linear algorithms, which is more pronounced when applied on large cardiac data sets.

A clear trend of cardiovascular MRI imaging is 3D imaging. In the case of cine imaging, the optimal solution is 3D imaging with all volumes acquired in a single breath-hold. The first advantage of this approach is that the number of breath-holds are reduced making the MRI procedure less fatigue for the patients, which is more pronounced in a clinical scenario with elder patients or patients with severe diseases. The second advantage of single breath-hold 3D cine imaging is that the acquired slices are perfectly aligned. In contrast, for repeated 2D slice imaging, the slices can be possibly mis-aligned due to patient motion between the breath-holds or different breath-hold states. Another strong advantage of 3D imaging is the simplified overall workflow, since the volumes can be acquired as non-angulated full-thorax images. Then, no slice angulation is required during the acquisition and MRI operators need less training and experience to perform a cardiac MRI exam. The slice angulation such as slices in short axis view can be performed during post-processing by reformatting of the 3D data. Alternatively, the

cardiovascular MRI analysis could be done directly in 3D leading to more accurate volume estimations. One goal of this thesis is to introduce and optimize a completely novel cardiac cine imaging method for the assessment of cardiac function in a single breath-hold. We present in this thesis “VF 3D-BRISA” (“Very Fast 3D Breath-hold Isotropic imaging using Spatio-temporal Acceleration”) and implement it on a 3T MRI system demonstrating acceleration factors of over 30 for cardiac cine MRI. The aim is to acquire all cardiac slices in a single breath-hold and performing whole-chest 3D cine imaging with minimal 3D slice planning.

All in all, cardiovascular MRI is an active field of research that still requires more image acceleration than has already been achieved, since the slice planning and acquisition in different breath-holds is a tedious and time-consuming procedure. Further acceleration enables whole-chest 3D cine imaging in a single breath-hold, which is investigated in this thesis.



## 2. Motivation and Objectives of the Thesis

### 2.1 Motivation

Cardiovascular disease (CVD) is the main cause of death in the European Union (EU) (47). Each year, 4 million deaths in Europe and 1.9 million deaths in the EU are caused by the consequences of a CVD (48). In clinical practice, patients with symptoms of a CVD are assessed with medical imaging for the diagnosis of the disease. Typical diagnostic parameters obtained by medical imaging are cardiac perfusion (ml/min/kg), Left Ventricle Mass (LVM), End-diastolic volume (EDV) and End-systolic volume (ESV) or stroke volume (SV). To obtain these values, a wide range of different diagnostic modalities are available, for example echocardiography, nuclear imaging, X-Ray, computed tomography (CT) or magnetic resonance imaging (MR).

The current gold-standard diagnostic technique for many cardiac parameters is Magnetic Resonance Imaging (MRI), due to its superb soft-tissue contrast and its high spatial resolution. Furthermore, MRI scans do not expose the patient with ionizing radiation which is potentially harmful to the tissue, unlike conventional X-Ray or CT. A new promising medical imaging technique with application also in cardiac imaging is Magnetic Particle Imaging (MPI), a new imaging technology invented by Philips Research Laboratories in 2005(1). In particular, MPI is a promising candidate for the measurement of dynamic parameters like cardiac blood flow and cardiac perfusion (in ml/min/kg), due to its high sensitivity and its potential for rapid imaging of up to 46 3D volumes per seconds, at a spatial resolution below 1 mm in a FOV of 20.4 x 12.0 x 16.8 mm<sup>3</sup> (2). A scan with these parameters is up to date yet quite hard to achieve with MRI due to its lack of imaging speed.

Imaging speed is crucial for these dynamic parameters, since the physiological uptake of the applied contrast agent in the heart tissue requires high image update rates. One approach to obtain cardiac perfusion with MRI is a dual bolus strategy (49) or a high-dose single-bolus acquisition(50,51). In the latter, the Arterial Input Function and cardiac muscle contrast uptake is measured by two different contrast boluses and are corrected for its non-linear saturation curve. However, a faster method like MPI would be beneficial for dynamic cardiac imaging, since the contrast dynamics can be resolved with higher temporal accuracy. Furthermore, the MPI signal strength is linear with the contrast concentration, making it feasible to measure the Arterial Input Function and cardiac muscle contrast uptake at the same time without any

corrections. However, since MPI is still in the preclinical evaluation phase, its application is not yet ready for clinical cardiac imaging and many limitations still need to be overcome until a human-sized MPI scanner will be available in clinics. One of these limitations is the currently small spatial coverage for in-vivo applications (small animals) with a Field-of-View (FOV) of only a few cubic centimetres. Insufficient spatial coverage prevents to measure both surrounding anatomy and cardiac perfusion at the same time. Thus, we propose to work on the development of methods for larger spatial coverage by extending the FOV during dynamic MPI acquisition, making it feasible to cover the anatomy of interest and its surrounding arteries and organs. This additional information can be used to improve image registration with high-resolution anatomic reference images to measure accurately the contrast dynamics in the heart muscle.

Although widely investigated during the last decades since its invention by Mansfield and Lauterbur in 1971(16), the application of MRI on cardiovascular imaging is still not widespread. One reason is the complexity of the scan procedure in MRI, requiring sophisticated slice planning to angulate the standard cardiac views, in which the cardiac parameters are typically measured. Another reason is the need for multiple breath-holds during image acquisitions to avoid image errors due to breathing movements. Thus, currently one to two slices are measured per breath-hold, which is an exhaustive task especially for patients of high age or patients with lung diseases. Consequently, there is a fundamental need for new imaging acceleration techniques acquiring all MRI data in a single breath-hold, preferably with an isotropic 3D resolution. Since improvements in imaging hardware are limited by physiological parameters like peripheral nerve stimulation and maximum RF energy disposition, the achievement of high acceleration factors is the key to cardiac 3D cine imaging.

## **2.2 Objectives**

The aim of this thesis is to develop new imaging strategies to improve cardiac assessment using non-invasive medical imaging. This goal has been divided in two different secondary objectives for improved evaluation of cardiac perfusion and cardiac function assessment.

First, we develop a method for improved assessment of cardiac perfusion, with a focus on Magnetic Particle Imaging (MPI). We investigate a way to improve the spatial coverage by extending the Field-of-View (FOV), which is currently limited to a few cubic centimetres for small animal sizes. For the assessment of cardiac perfusion in humans, the spatial coverage needs to be enlarged to cover both heart tissue and surrounding anatomy. We develop an FOV

extension method and optimize its acquisition parameters in simulations and phantom measurements at a preclinical MPI scanner at Philips Research, Hamburg, Germany.

The second aim is to develop a completely novel imaging method for the improved assessment of cardiac function. We introduce a new parallel imaging technique called VF 3D BRISA (“Very Fast Breath-hold Isotropic imaging using Spatio-temporal Acceleration”) and apply it to cardiovascular cine MRI, which will allow the assessment of cardiac function in a 3D single breath-hold acquisition. This has a strong advantage against conventional multi-slice 2D cine imaging which requires multiple breath-holds during the acquisition and scout planning scans. We show preliminary results of cardiac 3D cine imaging using VF 3D-BRISA and demonstrate the feasibility of this single-breath hold technique in humans. Additionally, we validate the proposed 3D technique in an in-vivo study at the National Center for Cardiovascular Research (CNIC) by comparison of VF 3D-BRISA cine imaging with the conventional multi-slice 2D cine imaging in an animal model (pig) with different degree of cardiac infarct size.

In the following areas, this work provides novel research:

- In the first part, a novel methodology for MPI is investigated that extends the spatial coverage during image acquisition. In the extended FOV, both cardiac function and surrounding anatomy like carotid arteries can be imaged. As a consequence, registration from the tracer medium-based MPI images to detailed CT or MRI anatomy reference scans is improved, which improves the quality of the cardiac perfusion assessment with MPI
- The second part is the introduction and implementation of a new image acceleration technique called VF 3D-BRISA for cardiac cine MRI. It is a combination of parallel imaging with a static tissue removal technique that provides high image acceleration factors, thus allowing cardiac function assessment in a single breath-hold.
- Since the image noise distribution is spatially inhomogeneous in parallel imaging in general, the noise enhancement of BRISA is studied in MRI simulations and real MRI data sets. As an output, limits and optimal imaging parameters for VF 3D-BRISA are obtained
- To demonstrate the feasibility of the novel technique, an in-vivo validation study is conducted in an animal model (pig). In this work, it is shown that 3D-BRISA measures cardiac function as accurate as conventional 2D multi-slice MRI and can thus be interchangeably used.

### **2.3 Outline of the document**

This document is divided into seven chapters. In Chapter 1, an introduction is given to medical imaging using MPI and MRI. Details and literature references are given about image generation, image reconstruction and practical challenges of MPI and cardiac MRI.

Chapter 2 presents the motivation and the objectives of the thesis.

Chapter 3 contains a proposed methodology to increase spatial coverage of MPI acquisitions and is compared to an existing method, and it is demonstrated that the proposed method leads to improved image quality at the cost of increased acquisition time.

In Chapter 4, a completely novel cardiac cine MRI imaging method is introduced called “VF 3D-BRISA” (“Very Fast 3D Breath-hold Isotropic Imaging using Spatio-temporal Acceleration”). The method is implemented on a 3T human MR system (Achieva 3T-TX, Philips Healthcare, Best, The Netherlands) and is demonstrated to reconstruct non-angulated 3D cine images acquired in a single breath-hold. Optimal imaging parameters for the method are derived in 2D and 3D experiments.

Chapter 5 deals with an in-vivo validation of the proposed VF 3D-BRISA methodology to assess cardiac function with 3D cine imaging. The method is validated against a reference method using multi-slice 2D cine imaging. Linear Correlation analysis and Bland-Altman plots show good correlation and agreement between the two methods and they can hence be used interchangeably.

In Chapter 6, an overall discussion is presented with main contributions and conclusions of the thesis. Future lines of research starting from this work are discussed. In Chapter 7, publications obtained from this work are presented.

## 3. Measurement of System Function with extended Field-of-View

### 3.1 Introduction

Magnetic Particle Imaging (MPI) is a new medical imaging technology which obtains dynamic images at high spatial and temporal resolution (1,2). In principle, there is no need for image reconstruction in MPI and the recorded signal can be mapped into the image domain, resulting in 3D images with high spatial resolution, in an approach called x-space MPI (52). However, this approach is currently limited to rather simple trajectories of the Field-Free Point (FFP). To date, more complex trajectories of the FFP require a reconstruction that involves inversion of a system function. To obtain a system function, a calibration scan is performed by moving a small delta-like sample point-by-point through each voxel of the final image and measuring the signal response. This area contains the Field-of-View (FOV) in MPI, to which we refer as the area which is covered by the FFP trajectory encoded by the oscillating drive fields. Since the size of the FOV is determined by the drive field amplitude and the magnetic field gradient, the size limit of the FOV is typically small for current MPI scanners due to SAR and nerve stimulation issues (9).

To cover a larger area, a concept has been introduced that acquires several adjacent FOVs, at the cost of decreased temporal resolution(53,54). In the latter, additional homogeneous offset fields, in MPI so-called focus fields, are applied step-wise to shift the center of the FOV, leading to increased volume coverage on several adjacent focus field stations. To this increased area we refer as “extended FOV”. In the next step, it has been experimentally demonstrated in (15) that signal encoding in MPI can be also done during the linear transit motion when the FOV is changed from one neighbouring focus field station to the other.

We investigate in this contribution a more complex motion of the FOV. We apply a complex FOV trajectory with two different acquisition strategies: In the first, a large system function is acquired that contains the extended FOV. In the second approach, we acquire a small system function of the FOV without a focus field sequence and apply the correction method proposed in (15) according to the applied FOV trajectory. For both approaches, we use simulations and a real MPI system with phantom measurements (Philips Research Laboratories, Hamburg, Germany).

With a continuous motion of the FOV on complex trajectories, sequences with large spatial coverage become possible with good performance in both spatial and temporal dimension. Further, one is not limited to stick to a static focus field station pattern and can adapt the sweeping path to have only desired regions in the final image, and thus the image acquisition time is only used for encoding of anatomic parts that are relevant for the current application.

### 3.2 Material and Methods

A sketch of the MPI field generator for the experiments in this paper can be found in(53). Two selection field magnets generate a single FFP in the center of the setup and a linear magnetic field gradient.

For the 2D experiments, two drive field coils are placed orthogonal around the center and generate a sinusoidal oscillating offset field. Thus, the FFP is shifted rapidly on a 2D Lissajous trajectory, which encodes a small rectangular FoV of:

$$\begin{bmatrix} FoV_x \\ FoV_y \end{bmatrix} = \begin{bmatrix} 2 \cdot H_{D,x}/G_x \\ 2 \cdot H_{D,y}/G_y \end{bmatrix} \quad (1)$$

with magnetic field gradients  $G_x$  and  $G_y$ , drive field amplitudes  $H_{D,x}$  and  $H_{D,y}$ . Thus, the size of the FOV encoded by the drive fields can be changed either by increasing the drive field amplitude or by decreasing the magnetic field gradient.

The focus field superimposes the drive field sequence with a sequence of time-varying homogenous offset fields, thus shifting the FOV in space. With magnetic offset field strength  $H_{FF,x}$  and  $H_{FF,y}$  of the focus field, the extended FoV has a size of

$$\begin{bmatrix} FoV_x \\ FoV_y \end{bmatrix} = \begin{bmatrix} 2 \cdot H_{D,x}/G_x \\ 2 \cdot H_{D,y}/G_y \end{bmatrix} + \begin{bmatrix} 2 \cdot H_{FF,x}/G_x \\ 2 \cdot H_{FF,y}/G_y \end{bmatrix} \quad (2)$$

at a potential cost of increased acquisition time for the additional focus field sequence. However, the acquisition time is not increased, when the same repetition times for the focus and drive field cycles is applied. In this work, we apply one focus field cycle in several drive field cycles.

#### 3.2.1 Complete System Function Acquisition

The common way to describe the imaging system in MPI is the characterization with a transfer function(55). Unlike the k-space formulation in Magnetic Resonance Imaging or Computed Tomography, there has not yet been found an equivalent mathematical theory to describe the 3D imaging process in MPI such as Fourier transform of the data.

Thus, the system is characterized by shifting a point-like sample of the contrast agent voxel by voxel through the extended FOV and measuring its signal response at each sample position. In the end, all information is collected to characterize the system of contrast agent, scanner properties and applied excitation sequence. One way to do the sample motion is by physical movement with a robot, as it was done in the first publication on MPI (1). It can also be done by means of the focus field, where the sample rests in the center of the MPI scanner and only the field configuration changes (56). In general, the measured signal response of one voxel is stored along one axis of the transfer matrix, in MPI called *system matrix*. This transformation matrix maps the distribution of the contrast agent to the acquired signal space, and the  $j^{\text{th}}$  column of the system matrix  $A$  can be acquired as

$$A_j = s_j \quad (3)$$

with the signal response  $s_j$  of the delta-like sample at the image voxel position  $j$ . With an unknown distribution  $\mathbf{c}$  of the contrast agent, the imaging equation can be written using the signal response  $\mathbf{b}$  from the phantom scan as

$$A\mathbf{c} = \mathbf{b} \quad (4)$$

Since the number of voxels can become large for a large and dense 3D grid, the number of columns and thus the time to acquire the complete system matrix can become long and may take up to one day. To accelerate the acquisition, several approaches have been proposed, such as using a simulated model (57) or a dedicated system calibration unit (56). Recently, a sparse acquisition of the system matrix has been proposed using compressed sensing (58). However, the best image quality has been so far reached by measuring a complete system matrix at all voxels, which is still the reference method for all strategies (59,60).

### 3.2.2 Correction Method

In the case of a combined focus and drive field sequence, a method has been proposed that recovers a system function of an extended FOV by a small system function with a FOV without focus sequence. The basic idea is to assign new spatial coordinates of the signal response from each voxel of the small system function according to the applied focus field trajectory. For FOV motion on straight lines, this method has been demonstrated to allow for the acquisition of images during a linear 3D- FOV motion of up to 1 m/s before significant artifacts arise(15).

For the correction method, first a small static system function is acquired with only a drive field sequence. If the columns in eq. (4) are stored in frequency-domain, an inverse Fourier transform needs to be applied to get a signal response in time-domain. Then, a coordinate transform of the

voxel coordinates is performed according to the time evolution of the focus field sequence, which is mathematically a row transform of  $A$ .

In the row transform, the rows in the corrected system function  $\tilde{A}$ , here denoted as  $\tilde{A}_i$ , are shifted according to

$$(A_i)_{0,1,\dots,N} \rightarrow (\tilde{A}_i)_{s(t),s(t)+1,\dots,s(t)+N} \quad (5)$$

with a small system function of  $N+1$  voxels. Before the row shift  $s(t)$  is applied, the matrix is extended with columns containing zeros to make sure that the shifted imaging region is still contained in the system function. A row shift induced by a linear one-dimensional focus field sequence can be written as

$$s(t) = \text{round}(2 \cdot H_{FF,x}(t)/G_x/s_x), \quad (6)$$

with the focus field offset  $H_{FF}$ , magnetic field gradient  $G_x$  and voxel size  $s_x$ . For non-linear shifts, for instance with a one-dimensional sinusoidal focus field sequence, the row shift is given by

$$s(t) = \text{round}(2 \cdot H_{FF,x} \sin(t)/G_x/s_x), \quad (7)$$

For higher-dimensional shifts, the index function has to be adapted according to the storage format of the columns. For the voxels outside the shifted FOV, the signal is zero-padded. At the border voxels between FOV and zero-padded region, a linear ramp with nearest-neighbour method is applied to suppress extrapolation artefacts. After the row transform, the columns of the system matrix are back transformed in frequency-domain for the reconstruction. In this contribution, we show that this correction method can be applied also on non-linear trajectories.

### 3.2.3 Image Reconstruction

For image reconstruction, a regularized least-squares approach is used with Algebraic Reconstruction Technique. Before the reconstruction step, the response spectrum is reduced using a signal-to-noise (SNR) measure as described in (61). After this reduction, the problem is solved as optimization problem

$$\|Ac - \mathbf{b}\|_2^2 + \|c\|_2^2 = \min! \quad (8)$$

The regularization parameter  $\lambda$  deals with the balance between improved SNR at the cost of reduced spatial resolution. In the reconstruction used in this paper,  $\lambda$  is chosen with a heuristic approach. Alternatively, it could be chosen using more sophisticated methods such as L-curve, see (62).

### 3.2.4 Simulations

An MPI field generator is simulated according to the one used in [6]. The field gradient is 1.25 T/m x 1.25 T/m in the horizontal plane, in which the phantom is placed. The drive fields are applied with frequencies of 24.15 kHz and 25.25 kHz at amplitudes of 14 mT. With these frequencies, the FFP is shifted rapidly on a 2D Lissajous trajectory, at a repetition time of 0.625 milliseconds [2] and a FOV of 2.2 cm x 2.2 cm.

For the focus fields, the complex trajectory is visualized in Figure 1. The focus field was applied with a sinusoidal sequence with amplitude of 16 mT, which results in a complex FOV trajectory of a closed 2D Lissajous cycle. The area covered by extended FOV is 4.8 cm x 4.8 cm. The area covered by the system function is 5.0 cm x 5.0 cm, containing the FoV motion. One focus field cycle is driven in two different acquisition times and thus in different average speed:

- One focus field cycle in ten drive field cycles (repetition time: 6.25 milliseconds, average FOV speed: 17 m/s)
- One focus field cycle in two drive field cycles (repetition time: 1.31 milliseconds, average FOV speed: 86 m/s)

In an optimized scanner, it would be possible to find drive field and focus frequencies that have same repetition time. However, in the constraints of currently available MPI systems the drive frequency is a fixed value and only the focus field frequency can be adapted. For the complete 2D system function, a region of 5.0 cm x 5.0 cm is discretized in 50x50 voxels at a spacing of 1.0 mm x 1.0 mm, in order to contain the FOV motion. To increase SNR of the system function, the focus field sequence is three times averaged for each voxel. For the small system function in the correction method, a system function with 30x30 voxel and 1.0 mm x 1.0 mm spacing is used, with three times signal averaging as well.

For the phantom scan, a Derenzo-like phantom is filled with Langevin particles of magnetic core diameter of 25 nm and 40 nm. The spacing is 1.2 mm - 1.6 mm - 2.5 mm - 3.5 mm - 4.2 mm. The dimension of the phantom is 4.8 cm x 4.8 cm. The simulations are performed by an internal software tool of Philips Research Hamburg, Germany.

### 3.2.5 Real MPI data

As MPI field generator, a preclinical MPI demonstrator is used at Philips Research Laboratories Hamburg, Germany. Its selection field consists in the horizontal plane of a magnetic field

gradient of 1.25 T/m x 1.25 T/m. The drive frequencies are 24.15 kHz and 25.25 kHz at amplitudes of 10 mT, resulting in an FOV of 1.6 cm x 1.6 cm. Due to current technical limitations for 2D imaging, the focus field was driven at 16 mT at an acquisition time of 160 drive field cycles per focus field cycle (repetition time: 1.04 s, average FOV speed 1.1 m/s). As is visualized in Figure 1c, the region of the extended FoV is 3.8 cm x 3.8 cm.

For the complete 2D system function, a region of 4.0 cm x 4.0 cm is discretized in 40x40 voxels at a spacing of 1.0 mm x 1.0 mm, containing the FOV motion. For the calibration sample motion, a focus field based system function is used as described in [8]. For each voxel, the focus field sequence is three times averaged to increase SNR. For the correction method, a small system function with 30 x 30 voxels is acquired at a spacing of 1.0 cm x 1.0 cm, with three times signal averages as well.

For the phantom, Resovist (Bayer Schering AG) is used as contrast agent at a concentration of 50 mM (Fe)/l. Resovist is the gold-standard MPI contrast agent and has comparable MPI performance to Langevin particles with diameter of 22 nm. The shape of the phantom is a Derenzo-like phantom with spacing between the holes of 1.0 mm - 2.0 mm - 3.0 mm - 4.0 mm.

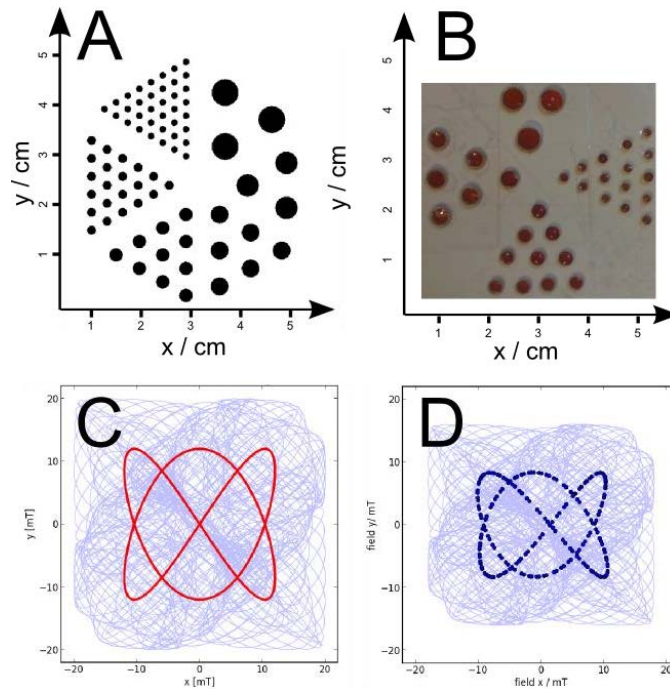


Figure 1. (A) Simulated Derenzo-like phantom with spacing 1.2 mm - 1.6 mm - 2.5 mm - 3.5 mm - 4.2 mm (B) Derenzo-like phantom used in the experimental validation, filled with Resovist (Bayer Schering AG), 50 mmol(Fe)/l. Spacing is 1.0 mm - 2.0 mm - 3.0 mm - 4.0 mm (C) Simulated complex focus field trajectory of the FOV (red), overlay with addition of the drive field (D) Measured complex focus field trajectory of the FOV (blue dots), overlaid with addition of the drive field.

### 3.3 Results

Several images were acquired and reconstructed with the combined focus field and drive field sequence. Figure 2 shows reconstructed simulated MPI images with different particle sizes and different trajectory speed of the FOV. For fast complex FOV movements (acquisition time: 1.31 ms, average speed: 86 m/s ) in the simulation, the tubes of 1.6 mm could be resolved in the Derenzo-like phantom with the approach to measure the complete system function ( Langevin particle diameter: 40nm). The approach with the correction method was able to resolve up to 2.5 mm in this case. For slower FOV movements (acquisition time: 6.25 ms, average FOV speed: 17 m/s), both approaches work equal.

With a smaller lambda factor in the regularization, the resolution is slightly improved for the complete measured system function resolution without compromises in image quality. With the same smaller lambda factor for the corrected system function, the reconstruction shows image artefacts.

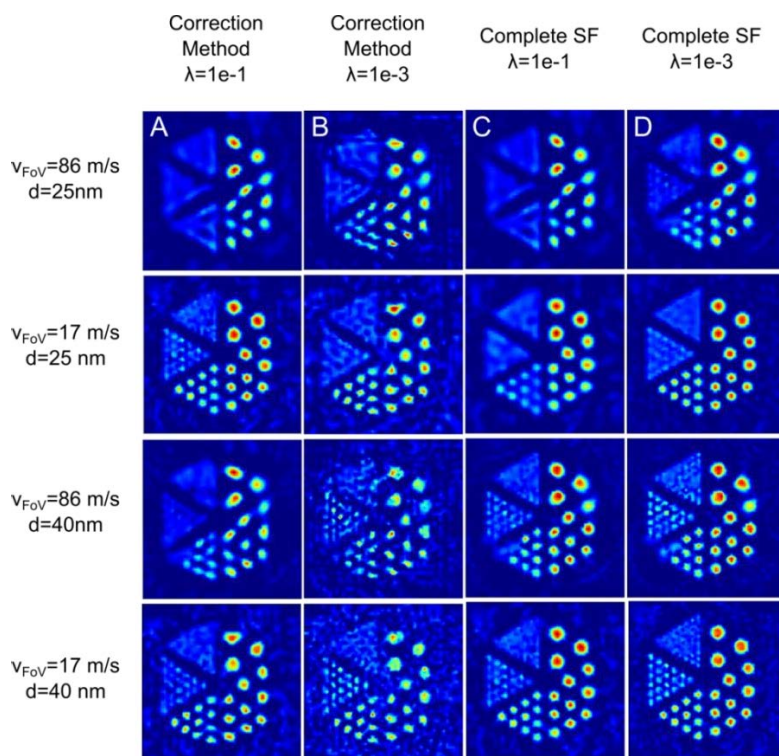


Figure 2. Simulation results at particle sizes of 25nm and 40 nm. Acquisition time is 1.25 ms for the fast trajectory (86 m/s FOV speed) and 6.25 ms for the slow trajectory (17 m/s FOV speed). The total extended FOV is 4.8 cm x 4.8 cm. In columns (A) and (B), the images are generated with the correction method for a small system function, see theory part II. In columns (C) and (D), images are generated with a complete system function of the extended

FoV. For the images in columns (B) and (D), a smaller lambda factor is used in the regularization.

For the real MPI data shown on Figure 3, we observed that the focus field amplitude was decreased, thus the phantom did not fit completely into the extended FOV. For the available FOV speed (acquisition time: 1.04 s, average FoV speed: 1.1 m/s), both approaches work equal.

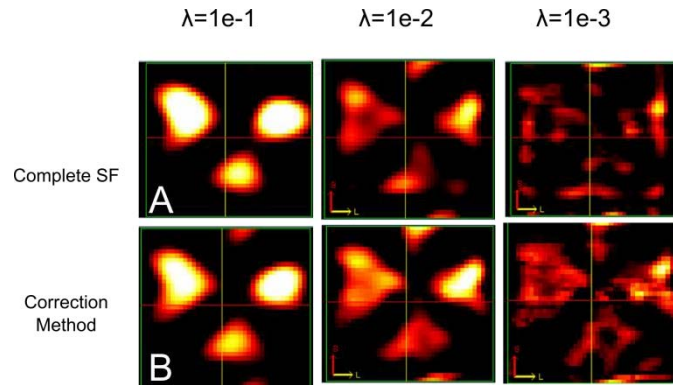


Figure 3. Reconstructed images from measurements at a preclinical MPI demonstrator. Acquisition time is 1.04 s for the complex trajectory. The total extended FOV is 3.8 cm x 3.8 cm. In row (A), the images are generated with a complete system function of the extended FOV at different lambda factors in the regularization. In row (B), the images are generated with the correction method for a system function with small FOV, see theory part II.

### 3.4 Discussion and Conclusion

Both acquisition schemes studied in this paper can be applied to cover an extended FOV with fast complex focus field trajectories. The correction method works well for slow FOV speed (17m/s). For high FOV speed (86 m/s), the image quality is slightly better for the completely acquired system function. The speed limit is lower in this contribution than in (15) taking into account that the 2D drive field repetition time is in fact 33 times shorter than for a 3D drive field and thus the speed limit is lower accordingly. Potential inaccuracies due to field inhomogeneities in extended FOV could affect the final reconstructed images in comparison with simple trajectories. Non-linearity of the selection field could potentially affect the resolution in the outer part of the imaging volume. Theoretically, the complete system function method could perform better than the correction method due to these variations are already

included in the acquired system function although further research needs to be done in this field. For future validation on a real MPI scanner, it would be interesting to implement 3D complex movements and a technical modification to enable higher FOV speed.



## **4. VF 3D-BRISA: Very Fast 3D BReath-hold Isotropic imaging using Spatio-temporal Acceleration for non-angulated whole-chest 3D cardiac cine MRI**

### **4.1 Introduction**

The standard clinical measurement of left-ventricular function by MRI involves time-consuming acquisition of a stack of at least 10-12 slices in short-axis and long-axis orientation. Typically one or two slices are acquired per breath-hold. In addition to the actual (accumulated) scan time, this introduces additional time for patient breathing recovery between the breath-holds. Moreover, patient bulk movement and the fact that the breath-holds are often not identical, results in misregistration between breath-holds, which can compromise estimates of left-ventricular function. For these reasons there is a great interest in developing a highly accelerated cardiac cine acquisition method that acquires the entire heart in a single breath-hold and with sufficiently isotropic spatial resolution to allow subsequent reformatting in any desired orientation. In general, cine imaging to assess cardiac motion consists of a multi-phase acquisition to capture multiple time windows of the cardiac cycle.

The past 10 years have witnessed many advances in MRI imaging acceleration techniques for cardiac cine applications (28,30,32,38,39,46,63–69). Parallel imaging techniques use receiver coil sensitivities in the reconstruction process to reduce the number of k-space profiles, reaching acceleration factors of up to 3 for 2D cine acquisitions (28,30). K-t acceleration techniques extract signal correlation from a low-resolution training dataset to recover omitted k-space profiles, achieving acceleration factors of up to 8 (38,63–65). The kat-ARC technique improves image quality of k-t acquisitions by adapting the local cardiac motion at each cardiac phase, (66,67). Compressed sensing techniques have been successfully applied to multi-slice cardiac cine imaging with an acceleration factor of around 11 (32,46,68).

A particular acceleration technique for cardiac cine imaging is NoQuist (43). In NoQuist, the FOV is divided into a static and dynamic image region based on prior anatomical knowledge. The signal from those static and dynamic image regions is modelled in a system matrix that simultaneously takes into account all acquired k-space data. Then, NoQuist reconstruction consists of inverting this system model matrix. The NoQuist technique has also been combined with parallel imaging (PINOT, Parallel Imaging and NoQuist in Tandem (44), which allows higher acceleration factors at the cost of an SNR penalty and an enlarged system matrix. In both

techniques, the maximum acceleration factor is limited by the size of the dynamic region in comparison to the entire FOV. This limitation is less pronounced in 3D acquisitions where the FOV reduction can be applied in two phase encoding directions. However, the computational complexity of the system matrix inversion becomes too computationally expensive in the case of 3D cardiac cine datasets.

In this contribution, the VF 3D-BRISA technique (Very Fast 3D BReath-hold Isotropic imaging with Spatiotemporal Acceleration) is presented for highly accelerated 3D cardiac cine imaging. BRISA shares with PINOT the idea of combining parallel reconstruction techniques with FOV reduction to a dynamic image region. However, BRISA substitutes the inversion of the large system matrix, as used in PINOT, by an extension of SENSE reconstruction algorithm.

## 4.2 Theory

BRISA consists of acquiring two different datasets in the same scan in an interleaved fashion with different SENSE acceleration factors (Fig. 1a, b). The first dataset (Fig. 1a) does not contain any temporal information and is obtained in a single-phase acquisition with relative low acceleration factor (E). The second dataset (Fig 1b) contains dynamic information and is obtained in a multi-phase cine acquisition with higher acceleration factor D ( $D > E$ ). The first (static) dataset is used to remove signals of static image regions in the second (dynamic) dataset (marked region in Fig. 1c). After the signal has been removed, the reconstruction FOV of the second dataset can be reduced to a smaller region, to which we refer to as “dynamic FOV” (Fig. 1c), since the outer image regions no longer contribute signal. In the example of Fig. 1c, the reconstruction FOV is reduced by a factor 4 ( $2 \times 2$  in LR and AP) compared with the entire FOV. As a result, the corresponding SENSE factor is reduced from 8 ( $4 \times 2$  in LR and AP) in the entire FOV to a SENSE factor of 2 ( $2 \times 1$  in LR and AP) in the dynamic FOV. The hypothesis of BRISA is that this reduction of the effective parallel imaging factor improves SENSE performance and reduces noise amplification.

Reconstruction in BRISA starts with the first dataset covering the entire FOV. This dataset is acquired with low acceleration factors and can be reconstructed using conventional SENSE (28) (Fig 2a). In this image, the dynamic FOV is selected by using prior knowledge about static and dynamic image regions. SENSE reconstruction of the first dataset provides an image corrected by the coil sensitivities(70). For BRISA, this image is weighted by coil sensitivities for each receive coil element to match the signal received by each coil element from the second dataset by voxel-wise multiplication (Fig 2b). The previous step produces synthetic (static) images equivalent to fully sampled images received by each coil element. The synthetic images are

masked out, by setting the pixels of the dynamic FOV to zero. After masking, only static image regions contribute to the signal of each coil element (Fig 2c, the region of masked pixels is indicated by dotted lines). These masked synthetic data are Fourier transformed to k-space and subsampled according to the subsampling factor  $D$  used in the acquisition from the second (dynamic) dataset. For better visualization, inverse Fourier transformed images of these data are shown in Fig 2d. The contribution of the static region to the signal is assumed to be constant during the cardiac cycle. Therefore, this signal can be removed from the data of the second dataset for every cardiac phase and coil element (Fig 2e) by direct subtraction of the matched k-space synthetic dataset (data shown in image space for clarity on Fig 2f). These new synthetic dynamic data only contain signal from the dynamic image regions, which allows a SENSE reconstruction with a smaller SENSE factor  $D^*$  (Fig 2g) in the reduced dynamic FOV. This reduction of the effective SENSE factor decreases the noise amplification and the geometry factor in the reconstruction of the second dataset (28).

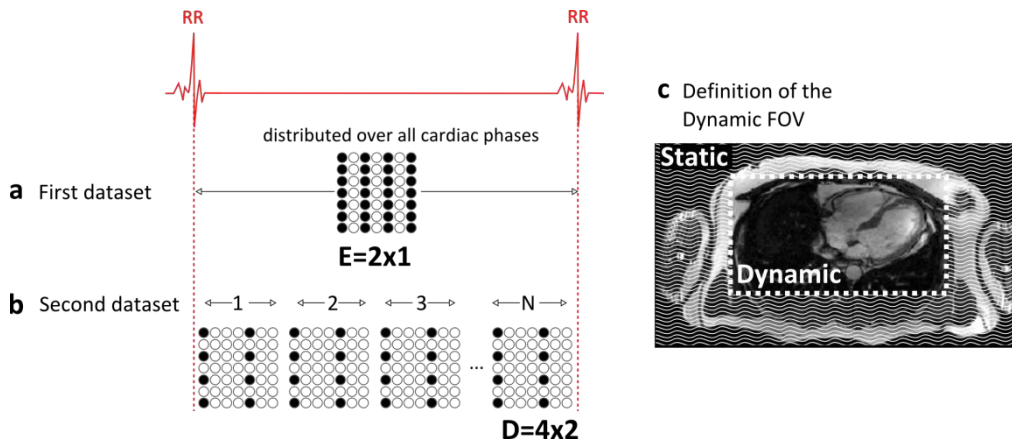


**Figure 1** (a+b) 3D k-space sampling for BRISA in an accelerated cardiac cine acquisition. The number of phase-encoding steps is reduced in 2 phase-encoding directions. Filled dots represent acquired k-space profiles and open dots represent k-space profiles that were not acquired. (a) Acquisition of a single 3D k-space for the first (static) dataset, acquired once throughout the cardiac cycle, with subsampling factor  $E$ . (b) Acquisition of 3D k-space data for the second (dynamic) cine dataset, acquired in every cardiac phase with a k-space subsampling of  $D=4 \times 2$ . (c) Definition of the dynamic FOV within a large FOV covering static and dynamic image regions.

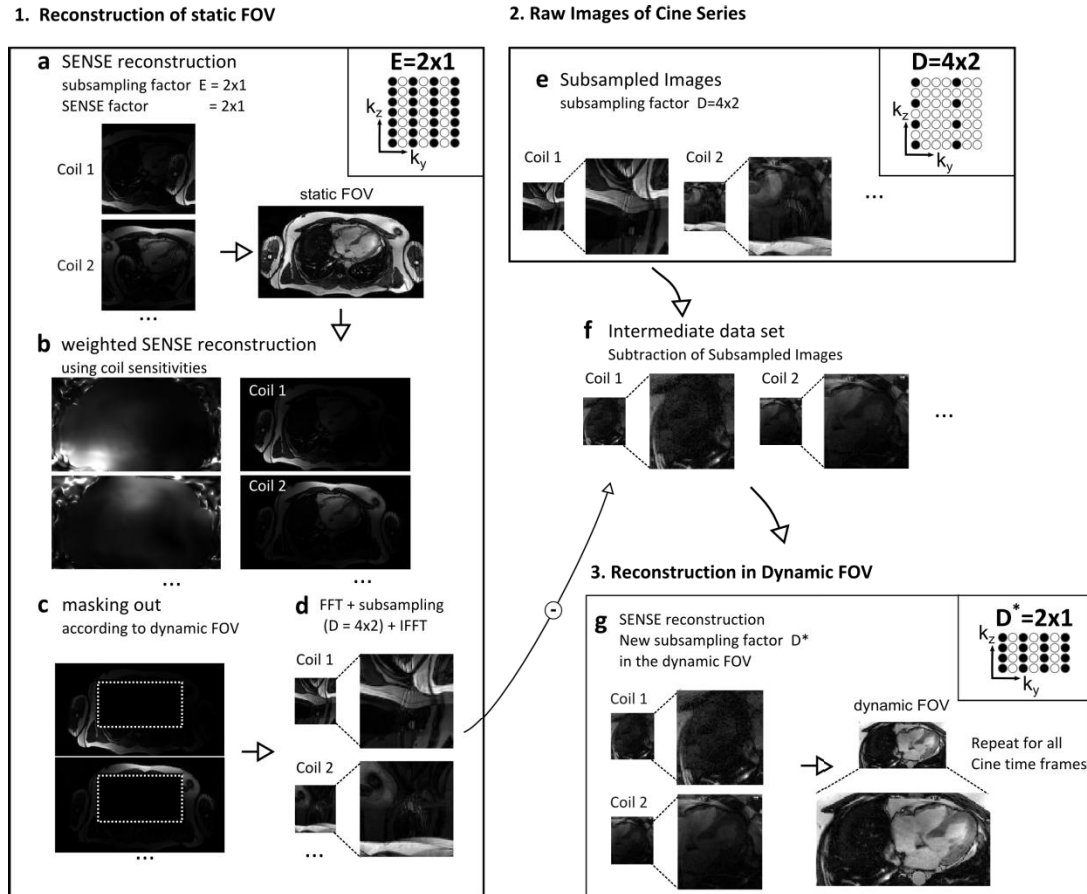


**Figure 2:** 3D-BRISA reconstruction steps. The left side shows the generation of the static tissue image for each coil; the right side shows the processing of the dynamic tissue signal. (a) Input coil images for the under-sampled static tissue image and SENSE reconstruction of the full FOV volume (with subsampling factor  $E$  in the full FOV). (b) Voxel-wise multiplication of the homogeneous full FOV volume by coil sensitivity maps of each receive coil. (c) Masking out of the dynamic FOV with zeros. (d) Undersampling of the masked images according to the  $k$ -space acquisition scheme (with subsampling factor  $D$  in the full FOV). (e) Data from cine series, containing signals from dynamic and static tissue, acquired with subsampling factor  $D$  in the full FOV. (f) Generation of an intermediate dataset by subtraction of data from steps d and e. (g) Using the intermediate dataset as input, SENSE reconstruction can unfold the dynamic tissue images inside the dynamic FOV in every cine time-frame (with a subsampling factor  $D^*$  in the dynamic FOV).

#### 4.2.1 Calculation of net acceleration for BRISA

The net acceleration of BRISA is measured, with respect to a fully sampled cine acquisition with  $N$  cardiac phases in the original (full) FOV, taken into account both individual acceleration strategies:

- The subsampling factor  $D$  (for each of the  $N$  cardiac phases in the first (dynamic) dataset, see Fig. 1b).
- The subsampling factor  $E$  (for the second (static) dataset, see Fig. 1a).

This leads to a net acceleration factor R of

$$R = \frac{N}{\frac{1}{E} + \frac{1}{D}} \quad (1)$$

Efficient sampling of the first dataset can reduce scan time at the expense of a decreased temporal resolution of cardiac cine acquisition (Fig. 3). The decreased temporal resolution is less critical in the diastolic part of the cardiac cycle and can be compensated later by view sharing reconstruction techniques (71). In the example of Fig. 3 every cardiac phase is acquired with the same acceleration factor D but in three diastolic cardiac phases (light grey squared in Fig 3) the k-space sampling is modified to acquire the required information for the first dataset. The data of these three cardiac phases are combined with one cardiac phase of the second (dynamic) dataset to generate the single k-space for the first (static) dataset. Following this k-space sampling pattern, BRISA acceleration factor can be formulated as:

$$R = \frac{N}{\frac{1}{E} + \frac{N-1}{D}} \quad (2)$$

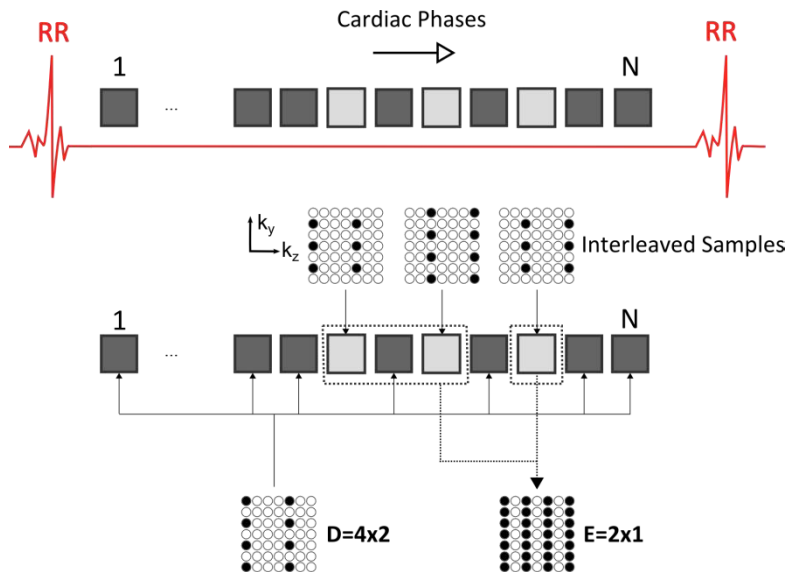


**Figure 3** Sampling of 3D k-space for BRISA at high acceleration during the cardiac cycle. The k-space data for the (dynamic) second dataset are acquired with a subsampling factor of  $D=4 \times 2$  in the entire FOV in  $N$  cardiac phases. Additional k-space samples are acquired for the first (static) dataset in 3 cardiac phases in diastole. After merging of all k-space data for the first dataset, a single (static) 3D k-space is generated for the full FOV volume with a subsampling factor of  $E=2 \times 1$ .

### 4.3 Methods

Three experiments were performed to validate the feasibility of BRISA. The first experiment was designed to evaluate noise amplification in the dynamic FOV. The second experiment was designed to compare BRISA with conventional SENSE reconstructions over a range of net subsampling factors. Finally, the third experiment was designed to evaluate BRISA feasibility on real 3D cardiac cases.

All experiments were performed with a 3T MRI system (Achieva 3T-TX, Philips Healthcare, Best, The Netherlands) using a 16-channel phased-array receive coil (SENSE XL Torso – 3.0 T Achieva, Philips Healthcare, Best, The Netherlands). The coil was configured with two 8 element coil layers (in AP direction), 4 coil element rows in LR direction, and 2 coil element rows in FH direction (65 cm L x 10 cm H x 45 cm W). The experiments were performed after obtaining written consent and approval from the local institutional review board. For the 2D experiments, no contrast agent was used. For the 3D experiments, the reduced blood-myocardium contrast in 3D excitation was compensated by acquiring images 10 minutes after injection of 0.2 mM/kg gadoterate meglumine (gadolinium-DOTA, marked as Dotarem, Guerbet S.A., Paris, France)((72).

For 2D experiments, theoretical noise amplification was assessed by geometric factor maps (g-maps) (1). For BRISA g-maps were computed inside the dynamic FOV with the virtual subsampling factor  $D^*$ . For the background, g-map values were taken from the first SENSE reconstruction in the full FOV using the subsampling factor  $E$ .

#### 4.3.1 Parallel Imaging in small Dynamic FOVs

The aim of this experiment was to assess the performance of parallel imaging reconstruction for different sizes of the dynamic FOV. For this experiment, one image was acquired from a single axial MRI slice at abdominal level, avoiding cardiac motion artifacts. Images were acquired with a 2D steady-state free precession technique (SSFP) (TR/TE/FA= 2.9ms/1.44ms/45°) with and FOV of 550x352mm (LRxAP), 2x2mm in-plane voxel size and 8mm slice thickness. Dynamic FOV size was chosen between 367 mm x 352 mm and 157mm x 141 mm (LR-AP). The data were acquired with a fully sampled k-space, and later subsampled in the phase-encoding direction and the readout direction in order to simulate the subsampled acquisitions used in BRISA for 3D acquisition. The subtraction of the signal from the static region in the BRISA reconstruction was performed from the same data set ensuring complete removal. Subsampling factor  $D^*$ , for the dynamic FOV, was kept constant at  $D^*=2 \times 2$  (RL-AP).

### 4.3.2 Comparison of SENSE and BRISA

The aim of the second experiment was to compare BRISA reconstruction with conventional SENSE reconstruction from the same cardiac triggered dataset. For this experiment, one image was acquired from a single axial slice at the level of the heart. Images were acquired by retrospective cardiac triggered 2D-SSFP (TR/TE/FA= 2.9ms/1.44ms/45°) with and FOV of 550x320mm (LRxAP), 2.6x2.6mm in-plane voxel size, 8mm slice thickness and 20 cardiac phases. Data were acquired with fully sampled k-space, and later subsampled in both the phase-encoding and readout directions in order to simulate 3D accelerated acquisition with BRISA and SENSE. Four k-space subsampling combinations of the acceleration factors D and E were used and shown on table 1, together with resulting net acceleration factors for BRISA and SENSE and dynamic FOV sizes. Q-body coil regularization was applied during reconstruction process in both cases (73). Total acquisition time in both techniques were equal although BRISA need to interleave three extra cardiac phases to generate the static information, producing less temporal resolution in the diastolic part of the cardiac cycle.

Subsampling Factor D	Subsampling Factor E	Net acc. factor R (BRISA)	Net acc. factor R (SENSE)	Dynamic FOV LR-AP (mm <sup>2</sup> )
2 x 2	2 x 2	3.8	4.0	275 x 160
4 x 2	2 x 2	7.6	8.0	275 x 160
6 x 2	3 x 2	11.4	12.0	183 x 160
6 x 3	3 x 2	16.3	18.0	183 X 213

**Table 1.** Reconstruction parameters for the second experiment. BRISA reconstruction uses the following parameters: SENSE subsampling factors D and E in the entire FOV, and dynamic FOV size. For BRISA, calculation of net acceleration takes account of D, E and number of cardiac phases. For conventional SENSE, the net acceleration factor is equal to the subsampling factor D.

### 4.3.3 Isotropic, non-angulated, whole-heart cardiac 3D cine imaging

The aim of the third experiment was to show the feasibility of VF 3D-BRISA to acquire single breath-hold whole-chest 3D SSFP cine acquisitions in humans. Non-angulated 3D coronal volume were acquired with, 300 x 520 x 310-316 mm FOV (FH-LR-AP), FA 42°, TR 2.4ms, TE 1.18ms (full echo), readout bandwidth =2160 Hz/pixel, Acquisition voxel Size 2.6x2.6x2.6 mm (reconstructed to 2.0x2.0x2.0 mm), 16 cardiac phases (retrospectively triggered), partial Fourier factors 0.7x0.7 (LRxAP), and elliptical k-space shutter; these parameters resulted in a scan time of 23-25 seconds (depending on heart rate and patient size). Non-selective RF excitation pulses were used to obtain a short TR while allowing relatively high flip angles. The

selected flip angle was chosen as a compromise between a short TR and the recommendations for cardiac SSFP imaging at 3T with contrast agents (74). To ensure homogeneous excitation RF shimming was applied (75).

Additionally, in all volunteers, 2D-SSFP reference cine images were acquired in a 2D multi-slice sequence with 12 breath-holds, in order to qualitatively compare the reformatted short axis from the 3D-BRISA acquisition with a standard cardiac cine MRI acquisition, with the following imaging parameters: FOV 380mm, FA 40°, TR 2.7ms, TE 1.3ms, readout bandwidth = 2016 Hz/pixel, acquisition pixel size 1.8x1.8mm, slice thickness 8 mm with no gaps, 30 cardiac phases, and scan time 10.4 seconds per slice

For cine acquisition in the entire FOV, a second (dynamic) dataset was acquired with a subsampling factor of  $D=6 \times 3$  (RL-AP), with respect to the original (full) FOV. For BRISA reconstruction, the size of the dynamic FOV was set at 173mm x 206 mm (LR-AP), and was reconstructed using a SENSE factor of  $D^* = 2 \times 2$  (LR-AP) in the dynamic FOV after subtraction of the signal from the static image regions. The acceleration factor E for the first (static) dataset was set to  $E=3 \times 1.5$  (LR-AP). Together with 3D partial Fourier of 49% (70% in LR and 70% in AP) and, 75% elliptical shutter the net acceleration, taking into account the subsampling factors D and E, was 34 (acceleration factor without partial Fourier and elliptical shutter was 15).

For the reconstruction of the first (static) dataset in the entire FOV, no regularization was applied. For the reconstruction of the second (dynamic) dataset in the reduced FOV, quadrature body coil regularization was used (73). Reconstructed 3D-BRISA images were transferred to Extended MR Workspace (Philips, The Netherlands) to perform double oblique multi-planar reconstruction (MPR) for short axes and 4-chamber orientations. Reconstruction time was measured excluding SENSE inversion matrix calculation, which can be computed beforehand.

## 4.4 Results

### 4.4.1 Parallel Imaging in small dynamic FOVs

The reconstructed magnitude images and g-factor maps for the 2D imaging experiment in the liver are presented in Fig. 4a. As can be seen in table 2, the max. G-factor value is 2.32 for the smallest FOV and 1.61 for the largest dynamic FOV size. In the images, slight noise amplification can be noted for small FOVs, but no image artefacts are visible.

Size Dynamic FOV / mm <sup>2</sup>	Max. G-factor
367 x 352	1.61
275 x 352	1.75
220 x 176	1.95
183 x 141	2.21
157 x 141	2.32

**Table 2.** Max. Values of g-maps for the SENSE reconstruction in different sizes of the dynamic FOV.

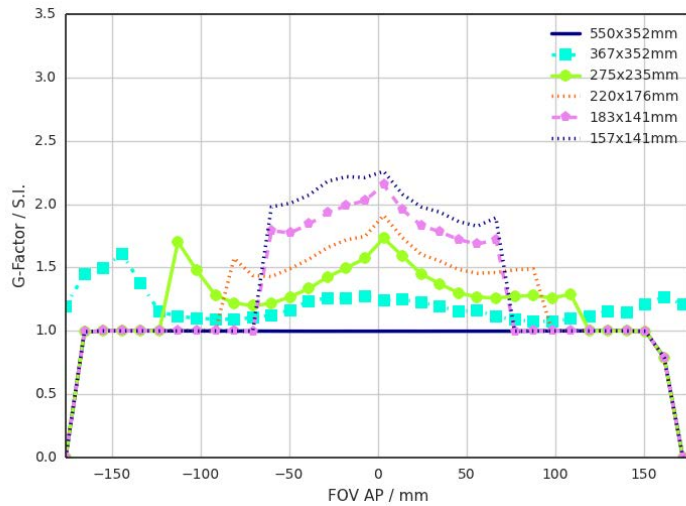
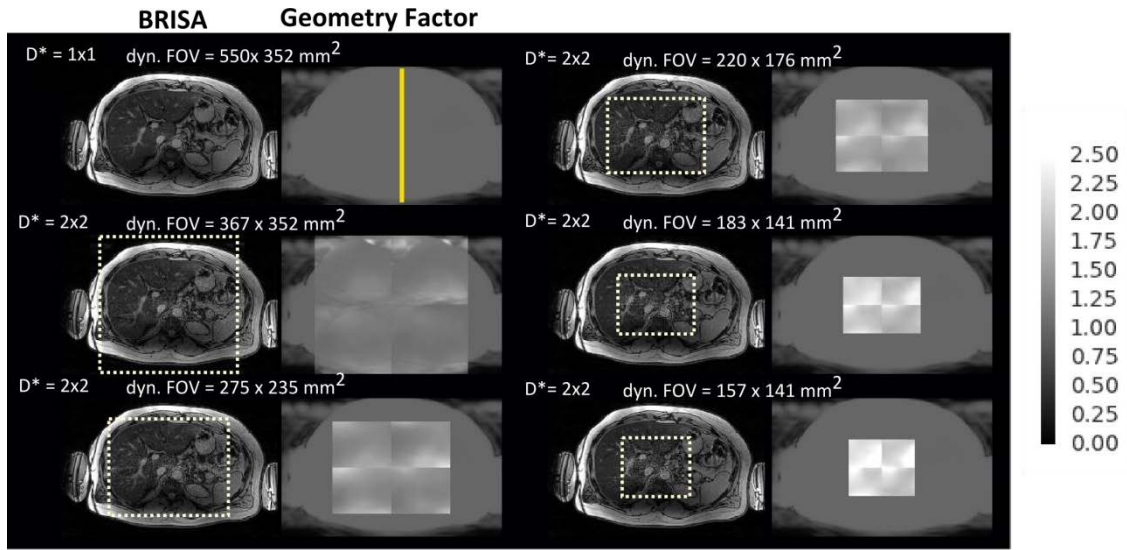


**Figure 4.** (a) BRISA reconstructions and g-factor maps for different-sized dynamic FOVs from a single acquired dataset. Dynamic FOV size is indicated above each g-factor map, starting at 550mm x 352 mm (top left) and decreasing to 157 mm x 141 mm (bottom right). Noise remained steady down to a FOV size of 200 mm x 176 mm (LR-AP). At FOV sizes below this, g-factor increased, resulting in greater noise enhancement. (b) Line profile taken from all g-factor maps along a line as indicated in Fig.4a on the g-factor image for dynamic FOV = 550 x 352 mm (top left). As can be seen in the profile plot, the g-factor

value increases from 1.0 (no SENSE) to a maximum of almost 2.5 for the smallest FOV of 157 x 141mm.

#### 4.4.2 Comparison of SENSE and BRISA

Fig. 5 presents the results of the comparison between BRISA and conventional SENSE reconstruction of the same 2D cardiac cine data set. A heart rate of 69 bpm lead to a temporal resolution of 44 milliseconds in the cine acquisition. It can be seen that conventional SENSE could be applied to this dataset with a subsampling factor up to  $D=4 \times 2$  (RL-AP) before the noise strongly increased, giving rise to image artefacts and high g-factor values (see table 3). For BRISA, the maximum subsampling factor in this dataset with acceptable image quality and g-factor values was a  $D=6 \times 2$  (RL-AP). Total reconstruction time in an off-line implementation was in the range of a few seconds for both methods (movie of the full cardiac cine cycle is available online as supplementary data, V1).

**FIGURE 5: Results of 2D Cardiac Cine Imaging Experiment**

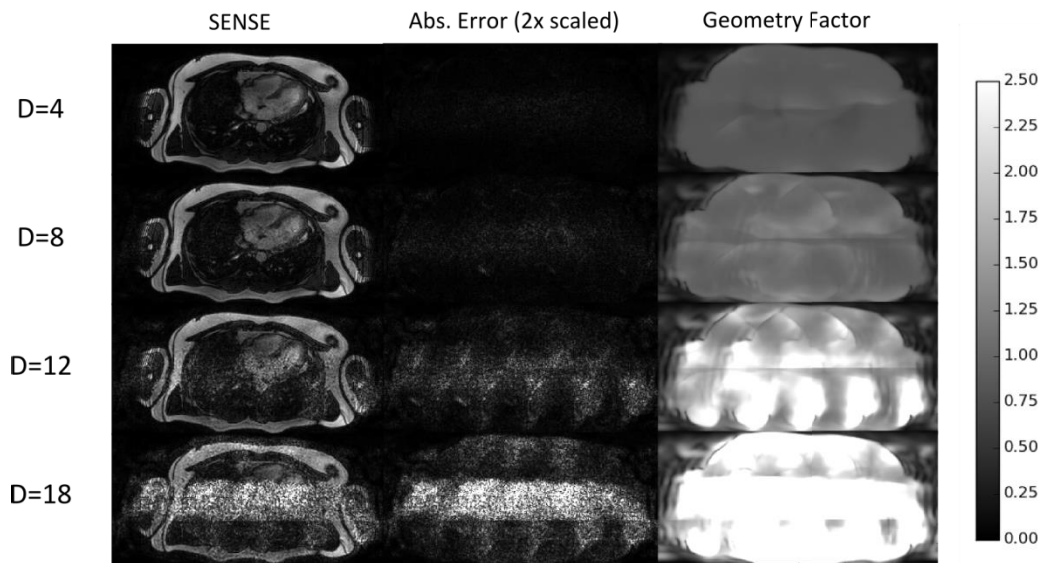
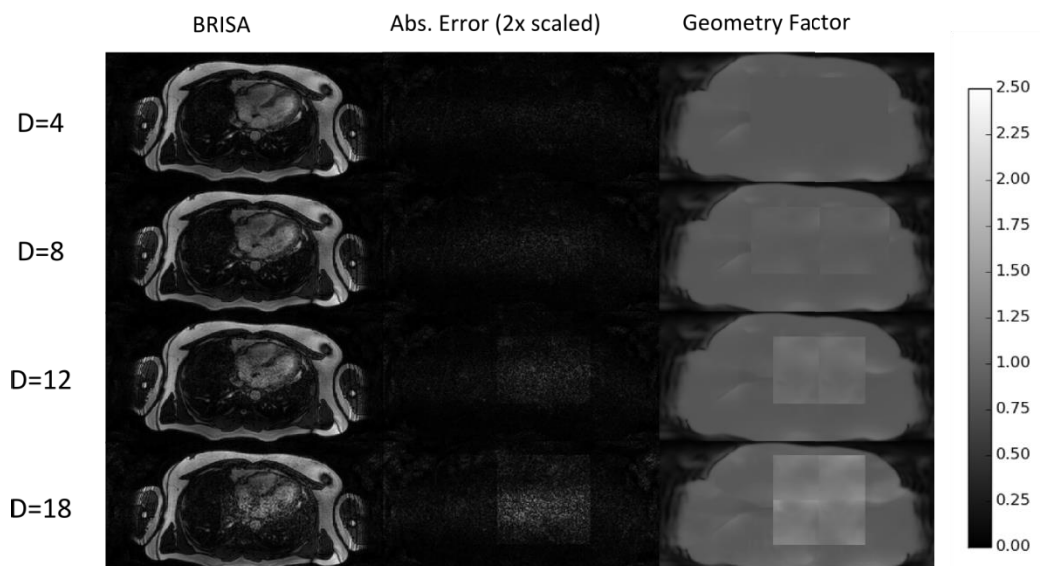
Subsampling Factor D	Max. G-factor BRISA	Max. G-factor SENSE	Dynamic FOV LR-AP (mm <sup>2</sup> )
2x2	1.28	1.27	275 x 160
4x2	1.29	1.79	275 x 160
6x2	1.35	6.18	183 x 160
6x3	1.77	8.80	183 X 213

**Table 3.** Max. Values of g-maps for BRISA and SENSE reconstruction for the second experiment.

#### 4.4.3 Isotropic, non-angulated, whole-heart cardiac 3D cine imaging

Three subjects were successfully scanned with BRISA, with a breath-hold of 23-25 seconds. The results for one of the patients using full-chest cardiac 3D cine acquisition with BRISA are shown in Fig. 6. Axial, Coronal and sagittal views (Fig 6a) show good image quality in systole and diastole with isotropic resolution and image contrast in all views. In addition reformatted 4 chambers and short axes view show proper cardiac contraction along the cardiac cycle.

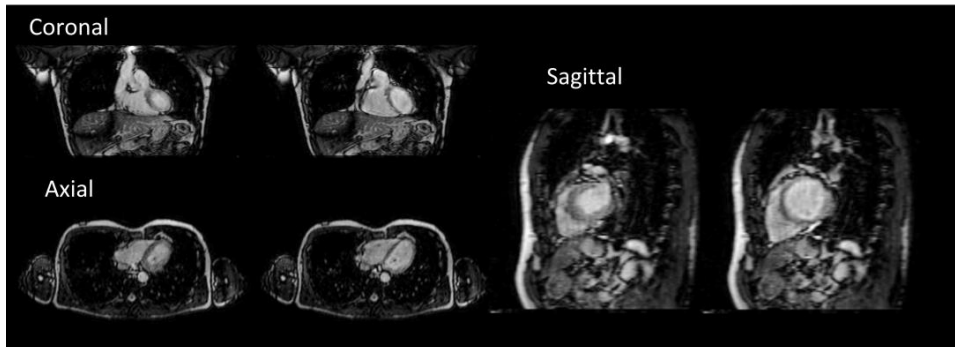
Reconstruction time for BRISA was 38.1 seconds for the complete 4D cine dataset on a single-core CPU in an off-line implementation (24.6 seconds for subtraction of static FOV information and 13.5 seconds for SENSE in the dynamic FOV). Videos of the full cine volumes are available online as supplementary data (V2-V4).

**a** Reconstruction with Conventional SENSE**b** Reconstruction with BRISA

**Figure 5.** 2D cardiac cine sequences reconstructed with BRISA (a) and conventional SENSE (b). The left column shows the magnitude images from the reconstruction. The middle column shows the absolute error for a fully sampled image, scaled by a factor 2 for better visibility. The right column shows the corresponding g-factor maps scaled between 0 and 2.5. BRISA could be applied to this dataset at up to 6x2 acceleration (RL-AP) and with a subsampling factor  $D=12$  before the noise enhancement strongly increased image artifacts and g-factor values. For conventional SENSE, the maximum subsampling rate with acceptable image quality and g-factor values was a 4x2 (RL-AP) and a subsampling factor  $D=8$ .

A stack of reformatted slices from BRISA-reconstructed 3D volumes from all three subjects are shown in Fig 7a-c. Images of the reference 2D multi-slice reference cine acquisition from a corresponding cardiac phase are presented together with the BRISA-reconstructed slices. For each participant, slices are presented in short axis.

**A** Center slices of 3D Cine imaging using 3D-BRISA



**B** Reformatted slices across cardiac phases

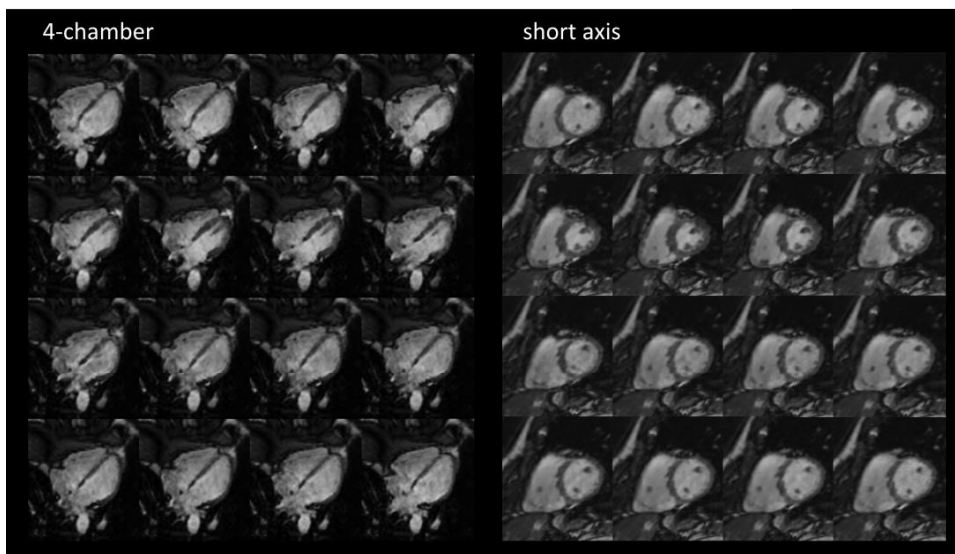


**Figure 6.** (a) Representative central slices of cine volumes from a non-angulated full-chest 3D cardiac cine acquisition, after reconstruction with 3D BRISA. For each orientation (axial, coronal, and sagittal), images were taken during systole (left) and diastole (right). (b) Reformatted images in 4-chamber view and short-axis view, which is typically the view in which cardiac function parameters are measured.

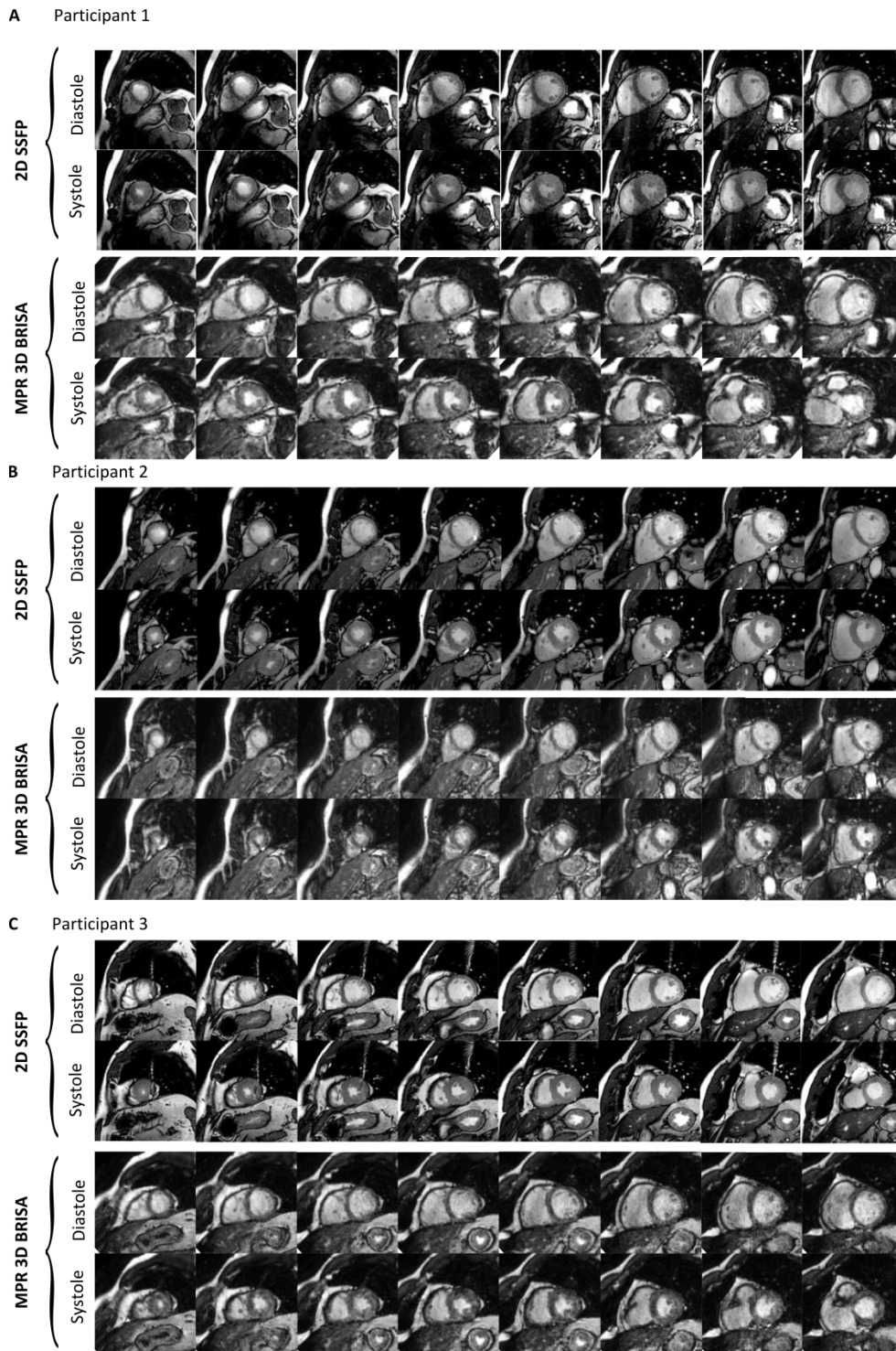


**Figure 7.** (a-c) 2D multi-slice cine MRI and reformatted stack of short axis slices of cine volumes from a non-angulated full-chest 3D cardiac cine acquisition and, after reconstruction with 3D BRISA for all three participants. One exemplary slice of a diastolic time point and one slice from a systolic time point is presented showing the cardiac muscle contraction.

## 4.5 Discussion

This study introduces the BRISA technique for whole-chest cardiac 3D cine imaging. BRISA achieved a high acceleration factor of over 30, enabling acquisition of good quality images in a 23-25 second breath-hold. Whole-chest acquisitions with high isotropic resolution allow the assessment of cardiac function and big vessel anatomy information like aorta and pulmonary veins. In addition, non-angulated coronal acquisitions remove the need for pre-scan scout images to find cardiac orientations shortening cardiac MRI workflow. Conventional parallel imaging techniques (28,30) cannot reach acceleration factors required to achieve this acquisition in a single breath-hold.

SENSE reconstruction fails when the number of unknowns (the number of aliasing pixels) is larger than the number of independent coil channels. In this case, the system of equations in SENSE is underdetermined and unfolding artefacts appear in the reconstructed images (see Fig. 6b with  $D=18$ ). With the coil topology used in the present study, SENSE is expected to reach a maximum acceleration factor of 8, because there are 4 coil rows in the LR direction and 2 coil layers in the AP direction, and the FH elements provide limited additional coil sensitivity information for SENSE reconstruction in AP and LR (see Fig 6a,  $D=8$ ). For an axial slice there are therefore 8 independent coil elements available that provide reliable information for generating images based on conventional SENSE (76). It is demonstrated that BRISA exceeded this SENSE limitation, as acceptable acceleration factors of BRISA were up to 12 ( $6 \times 2$  in AP-RL) (Fig. 6b). The key of BRISA is that all signal outside the dynamic FOV is removed and the dynamic information is reconstructed in considerably smaller dynamic FOV. In this situation, some of the aliasing pixels in a subsampled acquisition are located in empty areas (after the signal of static regions is removed), and these pixels can be safely excluded from the reconstruction (73). In other words, the parallel imaging factor is effectively reduced for these pixels when using appropriate regularization. In this way, BRISA allows acquisitions with a subsampling factor higher than is possible with conventional SENSE and even higher than the number of coil channels (see Fig 5b with  $D=12$  and  $D=18$ ).

The minimum size of the dynamic FOV for BRISA is determined by the need for it to encase the moving parts of the object in a cine acquisition. The use of parallel imaging in small FOVs (Fig. 5) showed that a SENSE reconstruction (SENSE factor of  $D^*=2 \times 2$ ) can be applied in a dynamic FOV as small as 200 mm x 176 mm (LR-AP) without noticeable reconstruction artefacts. Images with a dynamic FOV smaller than 183 mm x 141 mm (LR-AP) showed increased noise and correspondingly high g-factor values. Noise amplification in parallel imaging varies with position and depends on the coil geometry, the FOV, and the acceleration

factor (28). With the coil geometry used in this paper, the AP direction is the most sensitive to noise enhancement because there are 2 independent coil channels in that direction. When a small FOV is applied with parallel imaging in the AP orientation (which is the case with BRISA), the coil sensitivity functions become rather flat and the sensitivity inversion matrix becomes ill-conditioned for acceleration factors close to 2.

BRISA is suitable for non-slice selective 3D imaging acquisitions where the whole chest is excited. Non-selective pulses have three advantages: First, non-selective RF excitation pulses require less SAR, and have a simpler RF shape, leading to a shorter TR and therefore fewer SSFP off-resonance artefacts, which is an important issue at 3T. For the non-selective BRISA imaging presented in this paper, a TR of 2.4ms would increase to a TR of 4.4ms when using regular excitation pulses. Second, a shorter TR leads directly to faster acquisition times for the same number of phase-encoding steps. Third, with selective excitation, the actual 3D excitation and encoding thickness is always significantly larger than the final reconstruction, to compensate for the imperfect excitation profile. The potentially longer scan time required to encode a thicker 3D volume is largely compensated by the shorter TR and the fact that outer slices no longer need to be discarded with non-selective 3D excitation. A potential disadvantage of non-selective excitation is the need for a bigger slice-encoding thickness for static images in obese patients.

BRISA was successfully applied in 3D full-chest cardiac cine imaging in three participants. The sequence was tolerated without complications at good image quality. The 3D volumes of the cine series could be reformatted to short-axis and long-axis cardiac views using MPR during post-processing, and show motion information that is qualitatively equivalent to the reference 2D multi-slice standard (although at lower spatial resolution). Reconstruction of the complete 4D BRISA cine dataset took 38.1 seconds in a single-core off-line implementation. This fast reconstruction is possible because the algorithm is non-iterative and uses computationally simple operations such as multiplication and subtraction as an add-on to conventional SENSE reconstruction. In contrast, model-based inversion methods such as NoQuist and PINOT, as well as compressed-sensing approaches, use iterative reconstructions, making them challenging for current CPU hardware and preventing their use with large cardiac 3D cine datasets. By comparison, the reported reconstruction time for PINOT is 58 minutes for a 2D cine experiment (44). High complexity is also a feature of compressed sensing methods, and reported reconstruction times for these methods range from 10 minutes per slice (46) to 30 minutes for a complete 3D cine dataset (77).

In comparison with kat-ARC(78), BRISA uses a SENSE accelerated acquisition to recover the signal of static image regions. In contrast, kat-ARC requires to acquire a fully sampled k-space

to estimate the signal from static regions. Moreover, to estimate moving pixels, kat-ARC requires several fully sampled images at different positions in the cardiac cycle, while BRISA uses prior anatomical knowledge to define these regions and can acquire all cardiac phases with a high k-space undersampling.

## **4.6 Conclusion**

VF 3D-BRISA has demonstrated good-quality whole-chest 3D cardiac cine imaging in a single breath-hold. This has the potential to significantly improve clinical workflow, because non-angulated thick 3D volume planning is much simpler and faster than the planning of the double-oblique short-axis and long-axis angulations used for conventional cine acquisitions. In addition, short reconstruction time of VF 3D-BRISA could allow its rapid integration into routine practice with clinical MR scanners. Further clinical validation of the method is required.

## **5. In-vivo validation of non-angulated whole-heart cardiac cine imaging using VF 3D-BRISA**

### **5.1 Introduction**

Cardiac magnetic resonance (CMR) imaging is the gold-standard tool for the evaluation of cardiac anatomy and function because of its superb soft-tissue contrast and high spatial resolution(79). Analysis of the left ventricle, including measures of end-diastolic volume (LVEDV), end-systolic volume (LVESV), mass, and ejection fraction (LVEF), is of immense diagnostic and prognostic value (80). However, physicians and MR technicians face challenges in the daily clinical application of cine CMR. One of these challenges is the long scan time, which requires patients to hold their breath throughout most of the data acquisition sequences in typically 6-12 breath-holds (81). In addition, correct adjustment of plane orientations for cardiac slice angulation is technically demanding, requiring high levels of training for technicians and MR specialists. A technique for non-angulated 3D acquisition would simplify the cardiac MR protocol and reduce scan times, preferably to a single breath-hold

A number of strategies have been developed to reduce CMR scan times. Compressed sensing and k-t-acceleration have been applied to acquire multi-slice cine CMR in a single breath-hold, and their derived values indicate good agreement with conventional multi-breath-hold cine sequences (38,46,64,65,82). However, none of the reported acceleration techniques provides isotropic resolution, and the cardiac slices need to be angulated with scout planning sequences. In addition, k-t-accelerated methods require a separate breath-hold for the training data set, and the obtained images are sensible to blurring artefacts.

Recently, VF 3D-BRISA has been proposed for highly accelerated assessment of cardiac motion with 3D cine imaging in a single breath-hold (83). In this work, the obtained motion parameters of 3D cine imaging with VF 3D-BRISA are validated against a 2D standard in a porcine model. The goal is to demonstrate that the obtained cardiac function parameters agree between multi-slice 2D cine and the proposed VF 3D-BRISA cine imaging and that the cardiac values can be obtained with good reproducibility under both healthy and unhealthy conditions. Pigs with a wide range of LVEF values were included after induced myocardial infarction / reperfusion. The results from this work lay a strong preclinical fundament for a future validation of VF 3D-BRISA in humans.

## 5.2 Material and Methods

Non-angulated 3D cine imaging with VF 3D-BRISA was compared with a reference method using 2D multi-slice cine imaging. Both datasets were acquired in a set of 20 pigs with differing degrees of cardiac performance (from normal function to severe post-infarction LV dysfunction).

### 6.2.1 Animal Model

A total of 20 castrated male Large-White pigs weighing 30 to 40 kg started and completed the protocol and comprised the study population. The study was approved by the Institutional Animal Research Committee and conducted in accordance with recommendations of the Guide for the Care and Use of Laboratory Animals. The study included 10 healthy control pigs and 10 pigs subjected to closed-chest myocardial infarction (84).

### 6.2.2 Study Design

The study design is visualized on Fig. 1. The MRI datasets were acquired in a set of 20 pigs with differing degrees of cardiac performance from normal function to severe post-infarction LV dysfunction. 3D Cine imaging and reference multi-slice 2D cine imaging was performed in all pigs. After reconstruction of the 3D cine volumes with VF 3D-BRISA, multi-planar reformatting of short axis angulation was performed to prepare the standard input for cardiac analysis software. In both 2D and 3D, cardiac motion parameters were obtained, namely Ejection Fraction, LV diastolic and systolic volumes and LV mass.

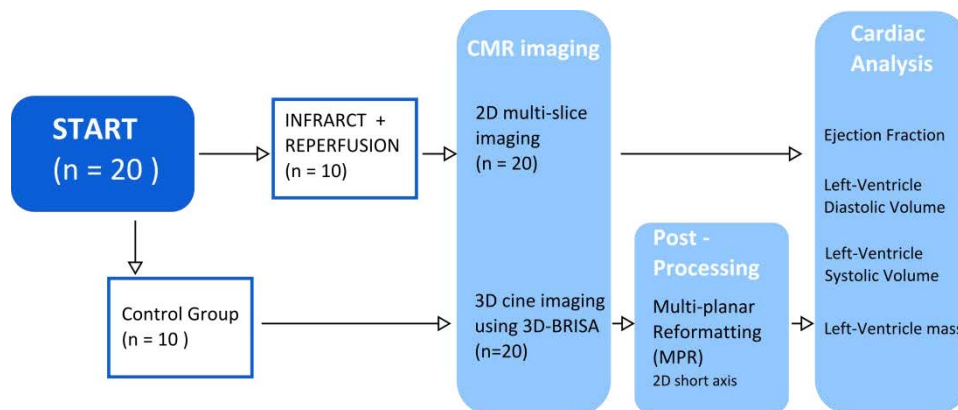


**Figure 1.** Study design of the in vivo validation 3D cine imaging with VF 3D-BRISA against standard 2D multi-slice cine imaging. The study consists of n=17 pigs, with n=12 pigs subject to myocardial infarction and reperfusion and a control group of n=5 healthy pigs. All animals underwent 2D and 3D cine imaging. After reformatting the 3D cine images from VF 3D-BRISA, cardiac parameters were measured in all pigs to obtain Ejection Fraction, LV systolic and diastolic volumes and mass.

### 6.2.3 CMR Protocol

CMR images in 3D and 2D were acquired with a 3T Achieva TX system (Philips Healthcare, Best, the Netherlands) equipped with 16-channel phased-array cardiac coil. Routinely, 2D-cine CMR images were acquired before gadolinium contrast administration (Gd-DTPA, Magnevist, Schering AG, Berlin, Germany). Multi-slice cine acquisition was based on a FFE-balanced steady-state free-precession sequence with the following parameters: field of view (FOV), 280 x 280 mm; voxel size, 1.8 x 1.8 mm; TR, 3.0 ms; TE, 2.0 ms; flip angle, 45°; reconstruction matrix, 172 x 170; number of cardiac phases, 30; number of excitations, 3. Initially, several scans were acquired to determine the correct short axis orientation of the 2D short-axis data set. The whole left ventricle was completely covered by 15-17 slices, with a slice thickness of 6 mm and no gap between slices. Acquisition time for the multi-slice 2D scans was 264 - 296 seconds. Approximately 10-15 minutes after gadolinium administration, a 3D FFE-balanced sequence was acquired in coronal orientation covering the whole chest from the diaphragm to the neck. The image volume was a FOV of 310x310x290mm<sup>3</sup>, with an acquired voxel size of 2.2x2.2x2.2mm<sup>3</sup> (TR = 2.3ms, TE= 1.15ms, flip angle 44°, acquisition matrix 140x141x132, with 16 cardiac phases) and partial Fourier factors of 0.7 in one phase-encoding direction and 0.7 in the other. The scans were ECG triggered with retrospective arrhythmia rejection under free-breathing conditions.

### 6.2.4 VF 3D-BRISA parameters

The dataset for the 3D cine images were acquired on an R=2x2 (RL-AP) subsampling grid and then additionally under-sampled to simulate an accelerated VF 3D-BRISA acquisition. As described (83) and (85), an additional static dataset is required for 3D-BRISA (which was initially published in (85) under the name “CASI-SENSE”, see Fig. 1). According to the reconstruction scheme of 3D BRISA, an additional (static) dataset was acquired on a Cartesian subsampling grid of *k*-space of R=4 (2x2 in RL-AP). The (dynamic) cine dataset was acquired on a Cartesian subsampling grid of *k*-space of R=4x4 (RL-AP). The size of the reduced dynamic FOV was chosen 155 mm x 155mm and reconstructed using a SENSE factor of 2x2 (RL-AP). Taking into account the partial Fourier acquisition of 0.49 (0.7x0.7 in AP-RL), a net reduction factor of R=27 (R=14 without partial Fourier) was reached with an equivalent acquisition time of 21-23 seconds (depending on heart rate). Image reconstruction was performed in an off-line implementation. The reconstruction CPU was a single-core workstation (3.6 GHz Intel(R) Xeon (R), 16 GB RAM, 64-bit Windows 7). The 3D cine volumes were interpolated to a final voxel size of 2.0x2.0x2.0 mm.

### 6.2.5 Data analysis

After 3D cine data reconstruction, the volumes were transferred to a workstation and reformatted to 15-17 short-axis slices using multi-planar reconstruction (MPR) to match the

slices from the multi-slice CMR sequence. CMR images were analysed with Cardiac Analysis software (MR Extended Work Space 2.6, Philips Healthcare, the Netherlands) by two observers experienced in CMR analysis.

The Blood-to-Myocardium ratio (BMR) and Contrast-to-Noise ratio (CNR) were measured as follows. A first ROI was placed in the septal region of the mid-ventricle to measure the signal intensity of the myocardium, and a second ROI was placed in the center of the left-ventricle to measure the signal intensity of the blood. The noise was measured as standard deviation in the corresponding ROIs. Then, the BMR was calculated as

$$\text{BMR} = \frac{S_{\text{blood}}}{S_{\text{myocardium}}}$$

and the CNR as

$$\text{CNR} = \frac{S_{\text{blood}} - S_{\text{myocardium}}}{0.5 \cdot (N_{\text{blood}} + N_{\text{myocardium}})}$$

### 6.2.6 Statistical analysis

Normal distribution was checked with graphical methods and a Shapiro-Wilk test. For quantitative variables showing a normal distribution, data are expressed as mean  $\pm$  standard deviation. For quantitative variables showing a non-normal distribution, data are reported as medians with first and third quartiles. Correlation and agreement of the functional variables obtained from 2D and 3D techniques was evaluated by Passing-Bablok regression (86), Intra-class coefficient (ICC) and Bland-Altman analysis (87). Bland-Altman analysis and ICC was performed to assess intra-observer variability. Statistical significance was set at a two-tailed probability level of 0.05. The authors had unrestricted access to the data and take responsibility for its integrity.

## 5.3 Results

In all 20 pigs, the VF 3D-BRISA sequence was applied successfully with no complications. The mean acquisition time of the 3D sequence was 21-23 seconds while the acquisition time for the 2D sequences was 264 - 296 seconds under free-breathing conditions. Reformatted short-axis views of the heart of a healthy pig with normal cardiac function are shown in Fig. 2a (videos are available in the supplementary data). Short axis views obtained from a pig four days after induced infarction in the anterior wall, followed by reperfusion, can be seen in Fig. 4b. The image quality of the reformatted 3D-cine imaging is comparable to that of the regular 2D-cine imaging.

Passing-Bablok regression comparison obtained by 3D- and 2D-cine imaging shows a high correlation and a good agreement, as can be seen on Figure 3. The values obtained by Bland-

Altman analysis for all cardiac parameters are shown on Figure 4 (see Table. 1,2). Table 3 shows the intra-observer variability for the repeated analysis of the 2D cine data set obtained by Linear Correlation and Bland-Altman analysis. Reconstruction time for all time frames of the complete 3D-cine dataset was 37-39 seconds. The blood-to-myocardium ratio (BMR) and the contrast-to-noise ratio (CNR) is shown on figure 5 demonstrating that the contrast is comparable between 2D and 3D BRISA.

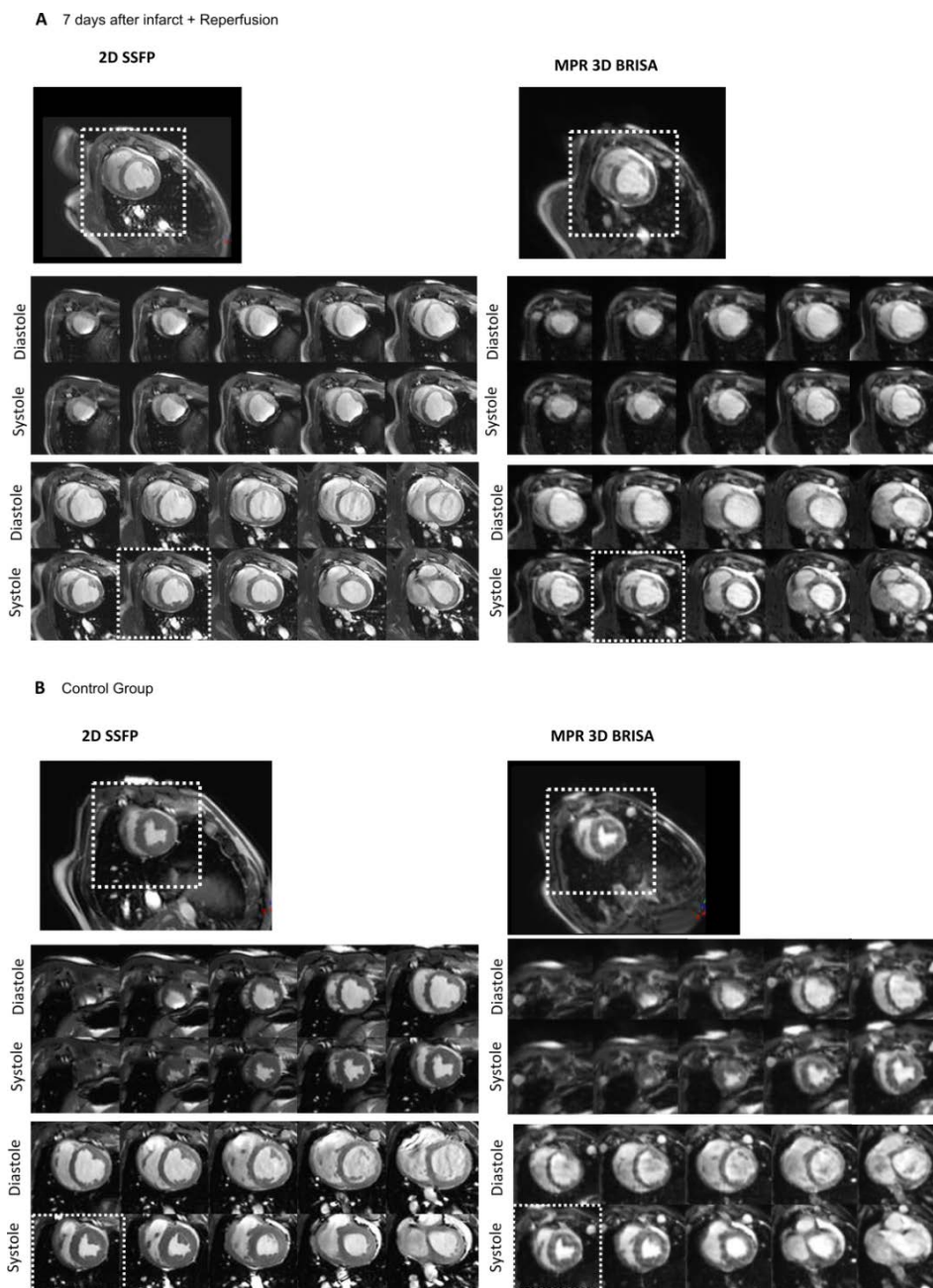


**Figure 2.** CMR cine imaging of the heart of (a) healthy pig with normal cardiac function (b) of the heart of an infarcted pig with impaired cardiac function (left) 2D multi-slice cine SSFP short axis views (right) Reformatted short axis views generated with BRISA in the same time frames. Image quality is comparable between the two acquisitions.

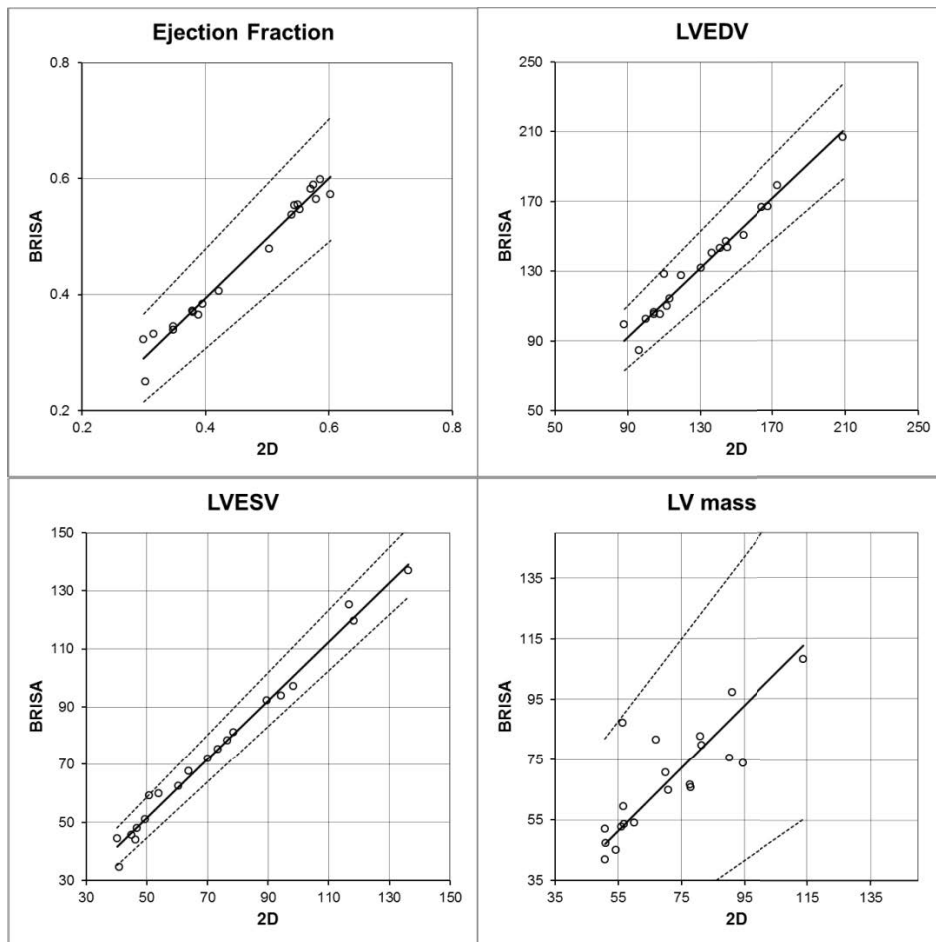


**Figure 3.** Statistical comparison of the values obtained with BRISA and 2D multi-slice cine SSFP acquisition sequences using Passing-Bablok regression. Data showing strong correlation between the two sequences for EF, LVEDV and LVESV; For LV mass, the variation is higher.

Parameter	Slope	Lower 95% CI	Upper 95% CI	Intercept	Lower 95% CI	Upper 95% CI	ICC
LV EF / %	1.03	0.91	1.12	-2.09	-5.95	3.02	0.98
LV EDV / ml	0.99	0.90	1.06	2.74	-7.04	14.15	0.96
LV ESV / ml	1.02	0.96	1.07	0.86	-3.52	4.72	0.98
LV mass / g	1.04	0.72	1.36	-5.79	-27.44	12.78	0.81

**Table 1.** Confidence-Intervals (CI) and slopes of the regression curve from the Passing-Bablok regression, and the Intra-class coefficient (ICC).

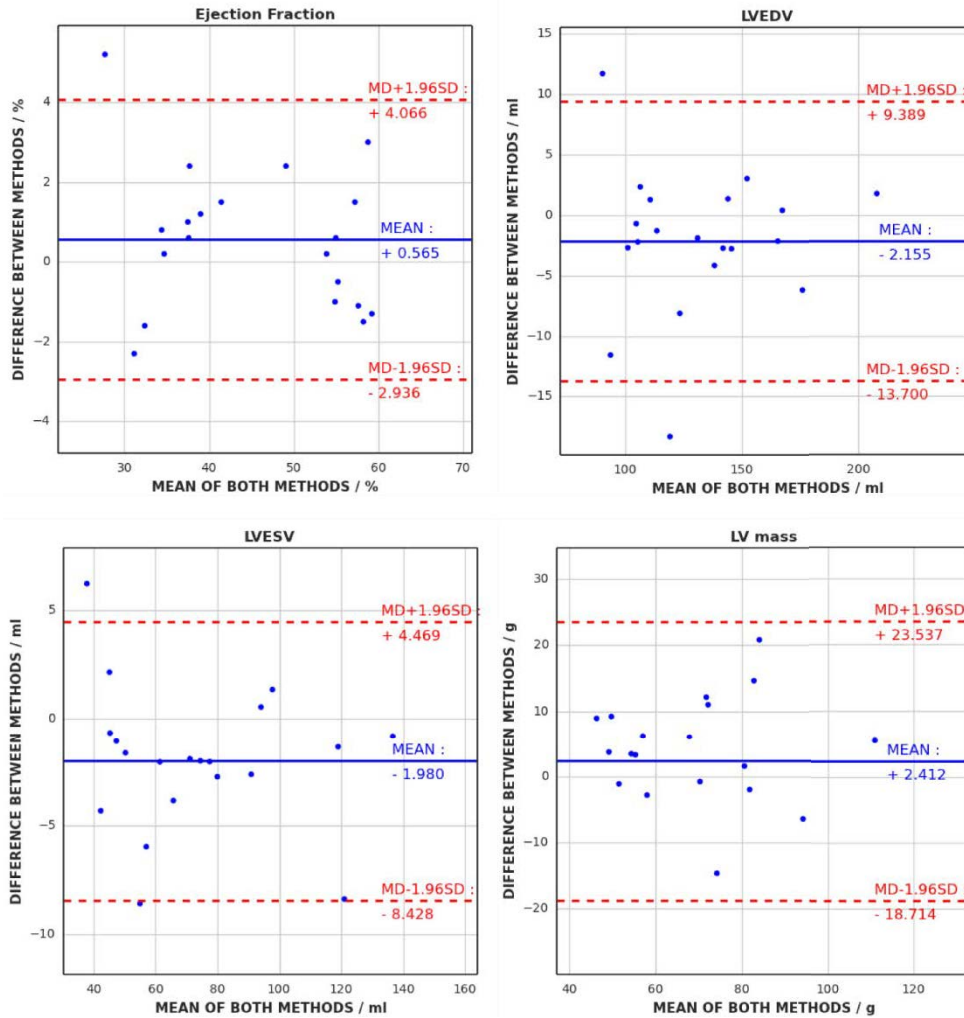


**Figure 4.** Statistical comparison of the values obtained for left-ventricular cardiac parameters with VF 3D-BRISA and 2D multi-slice cine acquisition sequences Bland-Altman comparison show good agreement for Ejection Fraction, Left Ventricle End-Diastolic Volume, Left Ventricle End-Systolic Volume and LV mass

Parameter	Mean 2D	Mean BRISA	MD	SD
LV EF / %	45.2 ± 10.9	44.6 ± 9.3	0.56	1.79
LV EDV / ml	131.9 ± 30.0	133.2 ± 30.1	-2.16	5.89
LV ESV / ml	73.9 ± 27.6	75.6 ± 28.0	-1.98	3.29
LV mass / g	71.1 ± 16.8	67.6 ± 16.9	2.41	10.78

**Table 2.** Bland Altman Analysis for the cardiac function parameters measured by 3D Cine and 2D Cine. Values are presented as mean ± standard deviation (SD) of the difference.

Parameter	Intra-observer		
	MD	SD	ICC
LV EF / %	0.20	1.20	0.98
LV EDV / ml	0.47	3.61	1.00
LV ESV / ml	-0.35	5.14	1.00
LV mass / g	-0.70	10.84	0.87

**Table 3.** Intra-observer variability, measured by ICC correlation analysis and Bland Altman.

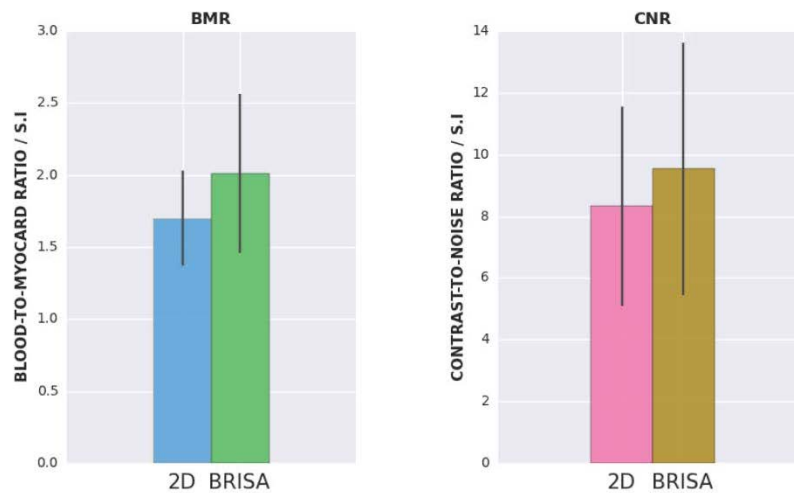


**Figure 5.** (a) Blood-to-Myocardium ratio (BMR) to measure the contrast between blood pool and cardiac muscle. (b) Contrast-to-Noise ratio (CNR) for 2D and BRISA, measured in a small ROI in a septal region of the mid-ventricle for the myocardium, and in the center of the left-ventricle at mid-diastole.

## 5.4 Discussion

In this work, we presented an in vivo validation of VF 3D-BRISA for the measurement of left-ventricular volumes and function. The values obtained show good correlation and agreement between the 3D-cine sequence with VF 3D-BRISA and the reference 2D multi-slice cine method (ICC > 0.81 for all 4 parameters). The 95% confidence interval (CI) for LV EF was -2.9% to 4.2%. Reported inter-observer reproducibility of LV EF measurements with standard 2D cine CMR is as high as 12.2%, reducible to 5.6% when an additional long axis scan is used (88). Thus, the agreement between the 3D- and 2D-cine methods is within the range of variation for the 2D-cine method itself. For LV mass, the results indicate that the VF 3D-BRISA provides

a slight underestimate (95 % CI: -11.5 g to 19.4 g). This arises from a less accurate definition of epicardial boundaries in the 3D images, particularly in the basal slices. Other 3D acceleration techniques feature a similar bias in LV mass measures, together with significant underestimation of LV diastolic volume (46,65). In line with this, the variability of 2D-cine imaging is also higher for LV mass (Table 3). The 3D-cine method estimates left-ventricular volumes without bias and with low variability (95 % CI: -10.4 ml to 7.83 ml for LV EDV; -7.6 ml to 4.2 ml for LV ESV).

Compared with reference multi-slice 2D cine imaging, the main advantage of VF 3D-BRISA is that the acquisition workflow is more straightforward, because the sequence is applied directly in a coronal view of the whole chest. Therefore, unlike standard multi-slice 2D cine, there is no need for additional scout sequences to angulate different cardiac views during the scan procedure. Though, the reformatting step of MPR of the volumes during post-processing led to additional time in data analysis in comparison with the multi-slice 2D images which are acquired directly in short axis. However, overhead time for 3D data analysis was in the range of several minutes to orientate and generate a stack of reformatted short axis slices. Additionally, this extra time did not block MR scan time.

The reconstruction time was 1.8 seconds per 3D volume, which is fast and convenient for many clinical situations that require fast image-based decision making. This efficiency is essentially a result that VF 3D-BRISA reconstruction is based on SENSE reconstruction, which has been previously confirmed to be solved rapidly (89). Hence, the whole 4D-cine dataset was reconstructed in 37-39 seconds, which is a reasonable time for a clinical application.

The acquisition time with the 3D sequence, 21-23 seconds, is much shorter than with 2D multi-slice cine (264 – 296 seconds), and in the range of a single breath-hold in patients. However, this already may extend the practical limit of reasonable breath-hold duration and may cause discomfort for the patient. Therefore, further research is required to further shorten the acquisition time for shorter breath-hold acquisitions.

One limitation of VF 3D-BRISA is that contrast administration is required to compensate strong signal saturation due to non-selective RF excitation pulses that reduce contrast between blood and myocardium (72). However, this is a minor limitation because many clinical cardiac MR protocols include contrast application for viability assessment of the myocardium by delayed contrast enhancement (90).

The main limitation of the study was that it was applied in a pig model, not in human study participants. However, the pig is an established model for heart studies because of the anatomical similarities of pig and human hearts. An unavoidable consequence of conducting the

study in pigs is that the sequence was applied under free-breathing conditions. This led to slightly decreased image quality seen as image blurring in both 2D and 3D cine imaging sequences. However, this study demonstrates that sufficient data can be collected in less than 21-23 seconds, which is within the upper range for a single breath-hold in humans.

## **5.5 Conclusion**

We have validated 3D cine imaging with VF 3D-BRISA in-vivo in a pig model for obtaining LV volumes and cardiac mass. The reformatted VF 3D BRISA cine images show considerable correlation and agreement with reference 2D multi-slice cine imaging. VF 3D BRISA has the advantage that it can be applied by less experienced operators and requires significantly shorter scan times than to acquire a stack of 2D short axis cine images. The proposed VF 3D BRISA sequence also provides reconstructions in fewer than 40 seconds, which is a suitable time for clinical evaluations. Further research is needed to validate VF 3D BRISA in humans under breath-hold conditions.

## 6. Discussion and Conclusion

The main goal of this doctoral thesis was to develop novel strategies for improved assessment of cardiac function using non-invasive medical imaging. Two main cardiovascular applications are in the focus of this thesis: cardiac perfusion imaging and cardiac function imaging.

Based on the obtained results in this thesis, the following conclusions are summarized:

1. After evaluating different approaches for increasing spatial coverage of Magnetic Particle Imaging (MPI), a method is proposed to reconstruct MPI images containing fast complex motions of the imaged area over a large volume. In simulations, good image quality was demonstrated reaching high spatial and temporal resolution.
2. A completely new image acquisition and reconstruction technique called “VF 3D-BRISA” has been introduced for 3D cardiac cine imaging using Magnetic Resonance Imaging (MRI). The proposed method is an extension of SENSitivity Encoding (SENSE) and is demonstrated to reach high acceleration factors (over 30) at good image quality. The high acceleration factor enables to acquire isotropic 3D cine cardiac sequences covering the whole-chest in a single breath-hold. Additionally, reformatting of different cardiac views can be performed as a post-processing step, shortening the actual overall cardiac scan time.
3. VF 3D-BRISA reconstruction has been simulated in 2D experiments and compared to conventional parallel imaging (SENSE), showing better image quality and less noise enhancement at higher acceleration rates when using BRISA. A study of spatially variant noise enhancement has demonstrated lower geometry factors using BRISA compared to conventional SENSE.
4. VF 3D-BRISA has been validated in-vivo for full-chest cardiac 3D cine imaging in an animal model (pig) against multi-slice cardiac 2D cine acquisition. Cardiac parameters such as Ejection Fraction, Left-ventricle volumes and mass show good correlation and agreement between 2D and 3D sequence.
5. VF 3D-BRISA has been implemented on a commercially available clinical 3T MR system. First applications on human volunteers demonstrate the feasibility of full-chest 3D cine imaging with VF 3D-BRISA in a single breath-hold. The obtained images

show good image quality and high contrast between blood and myocardium. Reconstruction time was in the 38.1 seconds for the complete 3D cine image dataset on a single-core CPU implementation.

MPI and MRI are at very different stages of its technical development. While MRI is established and widely applied in the daily cardiovascular clinical routine, MPI is currently at the stage of a research modality and its future preclinical and clinical role still needs to be defined. Due to its high spatial-temporal resolution, its high sensitivity and the linearity of the signal with contrast concentration changes, MPI is a promising candidate for cardiovascular applications such as cardiac perfusion imaging. MRI, in contrast, renders for applications on cardiovascular motion assessment due to its high soft-tissue contrast and its use of non-ionizing radiation.

With respect to the first cardiovascular application, high requirements are posed on a suitable imaging modality for cardiac perfusion imaging. One challenge is that high image update rates are required to capture the contrast perfusion dynamics. At the same time, sufficient spatial resolution is needed to distinguish blood pool and myocardium. As the arterial input function is measured for perfusion imaging, a linear relation between signal intensity and contrast agent concentration is desired. On one hand, MRI offers high soft-tissue contrast at high spatial resolution, yet one drawback is its low temporal resolution. A second obstacle for perfusion imaging with MRI is the non-linearity of the signal concentration with the MR signal, imposing mathematical and practical challenges to measure the arterial input function (51,91,92). In contrast to MRI, MPI renders for imaging of cardiac perfusion due to its high spatial and temporal resolution and the linearity of the signal with the contrast concentration. However, as MPI is a tracer-based modality, no soft-tissue contrast is visible in the images and the MPI images need to be registered to anatomic reference images to accurately calculate contrast perfusion of the myocardium.

In Chapter 3 a method is investigated with the goal to improve volume coverage of cardiac perfusion imaging with MPI maintaining high temporal resolution. For cardiac perfusion imaging with MPI, a compromise between FOV and temporal resolution needs to be taken. Larger volume coverage is desired to improve image registration with high-resolution anatomic reference tissue images. At the same time, high image update rates are required to capture the contrast perfusion dynamics. In Chapter 3, an FOV extension technique is proposed using a large system function covering complete motions of the FOV resulting in improved image quality at high temporal resolution, and it is compared with a time-domain correction method (15). However, one drawback of the proposed method is the large size of the extended system matrix, hence requiring much time for the calibration scan. The large number of calibration

samples leads to a time-demanding acquisition which is challenging for the use of MPI in routine cardiovascular applications. Additionally, the continuous use of the focus field system over a calibration time of several hours leads to high power demands since the current amplitude of the focus field generator is several hundreds of Ampere. To treat that issue, methods for shortening the calibration time will have to be applied. Several methods have aroused to shorten the acquisition time of the system function, such as simulating parts of the system matrix (57), using approximate solutions of the particle physics using Chebyshev polynoms (8), or the use of dedicated system calibration (SCU) units with high receive coil sensitivity, replacing robot movement of the calibration sample by the use of focus fields (56). Recently, Knopp et al. reported a more than 30-fold acceleration in acquisition of a compressed system function in a sparse domain by reconstructing missing entries using symmetry properties and Compressed Sensing reconstruction (58). All these acceleration methods or combinations of them may be used to shorten acquisition time of the extended system function of the proposed method, especially in the case of three-dimensional MPI with large spatial coverage. Alternatively, calibrations scans for the system function may be performed over night or during idle periods of the MPI system, since there is in theory no relationship between the time point of the object measurement and time point of the system function calibration scan.

With regards to the second cardiovascular application, cardiac cine imaging still remains a challenge since MRI is in principle a slow imaging method. To capture the heart motion with MRI, the conventional way is to segment the heart in multiple short-axes and long-axis slices and cardiac phases, and to acquire all cardiac phases of each slice in 10-12 separate breath-holds. The consequent need for multiple breath-holds and patient recovery prolongs the cardiac exam time and is a tedious and uncomfortable task for elder patients or patients with lung diseases. Additionally, the slice planning procedure of short-axis and long-axis angulation itself requires skilled MR operators and during the planning phase, while no clinically relevant information can be obtained. In Chapter 4, a completely novel method called “VF 3D-BRISA” was introduced and implemented to highly accelerate the assessment of cardiac function reaching acceleration factors of over 30. The high imaging acceleration opens the way to isotropic full-chest whole-heart 3D cine imaging in a single breath-hold. This procedure is advantageous and has impact on the cardiovascular application of MRI. Instead of slice planning in short-axis and long axis, volume planning for 3D cine imaging can be used which is simpler and faster since the volumes can be oriented in plain coronal orientation of the entire thorax without angulation. The angulation of short axis orientation can be performed during post-processing changing the whole workflow cardiovascular cine MRI. Alternatively, the angulation may be performed remotely via internet communication or by automatic procedures, see (93).

To replace conventional multi-slice 2D cine imaging by VF 3D-BRISA cine imaging in clinical cardiovascular practice, the obtained results of 3D cine imaging with VF 3D-BRISA need to be validated against the 2D standard. In Chapter 5, the results of an in-vivo study are presented validating multi-slice 2D cine MRI against 3D whole-heart cine MRI with VF 3D-BRISA in both healthy and unhealthy conditions. The study is conducted in an animal model of the pig closely resembling the human heart anatomy. We demonstrated that reformatted 3D volumes obtained by VF 3D-BRISA show a strong correlation and excellent agreement to multi-slice 2D cine imaging. This study was a close simulation of human cardiac function with cardiac infarct sizes of a wide range. Based on the preclinical research in this work, a strong fundament is laid to validate VF 3D-BRISA in a human study.

## **7.1 Future lines of research starting from the thesis**

Future possible work starting from this thesis may involve:

1. Application of the proposed FOV extension technique for MPI to in-vivo applications, such as cardiac perfusion imaging and image registration between MPI-MRI fusion images
2. The acquisition time of the proposed large system function may take much time especially for 3D MPI imaging. It will be interesting to combine the proposed method in this work with (57) or (58) acquiring model-based system functions or Compressed Sensing based system functions. In this way, the burden of long and power-demanding calibration scans of the system function is reduced for MPI imaging with continuous motion of the imaging volume.
3. After in-vivo validation in animals in this work, the next step is an in-vivo validation of VF 3D-BRISA in humans to compare the obtained cardiac function parameters with a reference multi-slice 2D cine SSFP sequence.
4. As the images are acquired in 3D, a direct 3D analysis of the cardiac parameters should lead to more accurate analysis of the cardiac function. So far, the 3D volumes were reformatted to short axis slices in 2D as input for the standard cardiac analysis workflow. A validation of direct 3D vs. reformatted 3D vs reference 2D cine CMR is a future step towards clinical routine.
5. Motion compensation of the chest due to breathing motion could be studied, for instance by the use of navigators to further improve image quality and to apply VF 3D-BRISA in a free-breathing acquisition

6. A parallelization of the reconstruction loop can be studied to further shorten reconstruction reaching real-time speed with multi-core implementations.
7. The k-space sampling pattern can be optimized such as in NoQuist (94) for an efficient sampling of the k-space data required for VF 3D-BRISA. Also, non-Cartesian trajectories can be investigated to enhance robustness against motion artefacts, however at the cost of increased reconstruction time and complexity.



## 7. Publications

### 7.1 Related to this thesis

#### Articles in peer-reviewed journals

- **Nothnagel ND**, Sanchez-González J. Measurement of System Functions With Extended Field-of-View. *IEEE Trans. Magn.* 2015;51:5100504. doi: 10.1109/TMAG.2014.2326253.
- Sánchez-González J, Fernandez-Jiménez R, **Nothnagel ND**, López-Martín G, Fuster V, Ibañez B. Optimization of dual-saturation single bolus acquisition for quantitative cardiac perfusion and myocardial blood flow maps. *J. Cardiovasc. Magn. Reson.* 2015;17:21. doi: 10.1186/s12968-015-0116-2.
- **Nothnagel ND**, Kouwenhoven M, Fernandez-Jiménez R, Desco M, Fuster V, Ibañez B, Sánchez-González J. VF 3D-BRISA: Very Fast 3D BReath-hold Isotropic Imaging using Spatio-temporal Acceleration for non-angulated whole-chest cardiac cine MRI. (submitted to *Magnetic Resonance in Medicine*)
- **Nothnagel ND**, Fernandez-Jiménez R, Gómez Talavera S, Gálan-Arriola C, López-Martín G, Desco M, Fuster V, Ibañez B., Sanchez-González J., “Volumetric non-angulated cardiac cine imaging with VF 3D-BRISA: A preliminary study with a porcine model” (in preparation)

#### International Conferences

- **Nothnagel ND**, Fernandez-Jiménez R, López-Martín G, Desco M, Fuster V, Ibañez B., Sanchez-González J., “CASI-SENSE: A novel reconstruction strategy for 3D single breath-hold isotropic cine imaging Background. In: *ISMRM, 23rd Annual Meeting: Toronto Canada. International Society for Magnetic Resonance in Medicine.* ; 2015. p. 3131.
- **Nothnagel ND**, Sanchez-González J. Measurement of System Functions With Extended Field-of-View. In: *4th International Workshop on Magnetic Particle: Berlin Germany (2014).*

## Patent Applications

- Sanchez-González J., **Nothnagel ND**, Ibañez B., Fernandez-Jiménez R, Fuster V. “Method and system for generating MR images of a moving object in its environment”. PCT/EP2015/072756 (2015)

## 7.2 Other publications

### Articles in peer-reviewed journals

- **Nothnagel ND**, Rahmer J. , Gleich B., Halkola A., Buzug T.M., Borgert J. “Steering of Magnetic Devices with a Magnetic Particle Imaging System”. IEEE Trans. Biomed. Imag. 2016; 99: doi: 10.1109/TBME.2016.2524070

### International Conferences

- **Nothnagel ND**, Rahmer J. , Gleich B., Halkola A., Buzug T.M., Borgert J. “Steering of Magnetic Devices with a Magnetic Particle Imaging System”. In: 3rd Internatinal Workshop on Magnetic Particle: Berkely, CA, USA (2013)

## 8. Bibliography

1. Gleich B., Weizenecker J. Tomographic imaging using the nonlinear response of magnetic particles. *Nature* 2005;435(7046):1214–7. Doi: 10.1038/nature03808.
2. Weizenecker J., Gleich B., Rahmer J., Dahnke H., Borgert J. Three-dimensional real-time in vivo magnetic particle imaging. *Phys Med Biol* 2009:L1–10. Doi: 10.1088/0031-9155/54/5/L01.
3. Knopp T., Buzug TM. *Magnetic particle imaging: An introduction to imaging principles and scanner instrumentation*. vol. 9783642041. 2012.
4. Sattel TF., Knopp T., Biederer S., et al. Single-sided device for magnetic particle imaging. *J Phys D Appl Phys* 2008;42(2):022001. Doi: 10.1088/0022-3727/42/2/022001.
5. Weizenecker J., Gleich B., Borgert J. Magnetic particle imaging using a field free line. *J Phys D Appl Phys* 2008;41(10):105009. Doi: 10.1088/0022-3727/41/10/105009.
6. Knopp T., Rahmer J., Sattel TF., et al. Weighted iterative reconstruction for magnetic particle imaging. *Phys Med Biol* 2010;55(6):1577–89. Doi: 10.1088/0031-9155/55/8/C01.
7. Dax A. On Row Relaxation Methods for Large Constrained Least Squares Problems. *SIAM J Sci Comput* 1993;14(3):570–84. Doi: 10.1137/0914036.
8. Rahmer J., Weizenecker J., Gleich B., Borgert J. Signal encoding in magnetic particle imaging: properties of the system function. *BMC Med Imaging* 2009;9:4. Doi: 10.1186/1471-2342-9-4.
9. Saritas EU., Goodwill PW., Zhang GZ., Conolly SM. Magnetostimulation limits in magnetic particle imaging. *IEEE Trans Med Imaging* 2013;32(9):1600–10. Doi: 10.1109/TMI.2013.2260764.
10. Schmale I., Rahmer J., Gleich B., et al. First phantom and in vivo MPI images with an extended field of view. *SPIE 7965*. SPIE Proceedings; 2011.
11. Rahmer J., Gleich B., Bontus C., et al. Rapid 3D in vivo magnetic particle imaging with a large field of view. *ISMRM, 19th Annual Meeting, International Society for Magnetic Resonance in Medicine*. 2011.
12. Rahmer J., Gleich B., Schmidt J., et al. Continuous Focus Field Variation for Extending the Imaging Range in 3D MPI. *International Workshop on Magnetic Particle Imaging (IWMPI)*. 2012.
13. Rahmer J., Gleich B., Weizenecker J., et al. Fast continuous motion of the Field of View in Magnetic Particle Imaging. *Int Work Magn Part Imaging* 2013;9(2011):5522.
14. Rahmer J., Gleich B., Schmidt J., et al. Increased Volume Coverage in 3D Magnetic Particle Imaging. *Proceedings of the 4th International Symposium on Applied Sciences in Biomedical and Communication Technologies*. ACM. 2011.
15. Rahmer J., Gleich B., Weizenecker J., et al. Fast continuous motion of the field of view in

- magnetic particle imaging. International Workshop on Magnetic Particle Imaging (IWMPPI). 2013.
16. Lauterbur PC. Image Formation by Induced Local Interactions: Examples Employing Nuclear Magnetic Resonance. *Nature* 1973;190–1. Doi: 10.1038/242190a0.
  17. Mansfield P., Maudsley AA. Medical imaging by NMR. *Br J Radiol* 1977;50(591):188–94. Doi: 10.1259/0007-1285-50-591-188.
  18. Vandenberghe S., Marsden PK. PET-MRI: a review of challenges and solutions in the development of integrated multimodality imaging. *Phys Med Biol* 2015;60(4):R115–54. Doi: 10.1088/0031-9155/60/4/R115.
  19. Chikazumi S. *Physics of Ferromagnetism*. vol. 1. 1997.
  20. Glover GH. Simple analytic spiral K-space algorithm. *Magn Reson Med* 1999;42(2):412–5. Doi: 10.1002/(SICI)1522-2594(199908)42:2<412::AID-MRM25>3.0.CO;2-U.
  21. Rasche V., De Boer RW., Holz D., Proksa R. Continuous radial data acquisition for dynamic MRI. *Magn Reson Med* 1995;34(5):754–61. Doi: 10.1002/mrm.1910340515.
  22. Fannjiang AC. The MUSIC algorithm for sparse objects: a compressed sensing analysis. *Inverse Probl* 2011;27(3):035013. Doi: 10.1088/0266-5611/27/3/035013.
  23. Wang Z., Arce GR. Variable density compressed image sampling. *IEEE Trans Image Process* 2010;19(1):264–70. Doi: 10.1109/TIP.2009.2032889.
  24. Fessler JA. On NUFFT-based gridding for non-Cartesian MRI. *J Magn Reson* 2007;188(2):191–5. Doi: 10.1016/j.jmr.2007.06.012.
  25. Knopp T., Kunis S., Potts D. A note on the iterative MRI reconstruction from nonuniform k-space data. *Int J Biomed Imaging* 2007;2007. Doi: 10.1155/2007/24727.
  26. Ham CLG., Engels JML., Van de Wiel GT., Machielsen A. Peripheral nerve stimulation during MRI: Effects of high gradient amplitudes and switching rates. *J Magn Reson Imaging* 1997;7(5):933–7. Doi: 10.1002/jmri.1880070524.
  27. Feinberg DA., Hale JD., Watts JC., Kaufman L., Mark A. Halving MR imaging time by conjugation: demonstration at 3.5 kG. *Radiology* 1986;161(2):527–31. Doi: 10.1148/radiology.161.2.3763926.
  28. Pruessmann KP., Weiger M., Scheidegger MB., Boesiger P. SENSE: Sensitivity encoding for fast MRI. *Magn Reson Med* 1999;42(5):952–62. Doi: 10.1002/(SICI)1522-2594(199911)42:5<952::AID-MRM16>3.0.CO;2-S.
  29. Sodickson DK., Griswold MA., Jakob PM. SMASH imaging. *Magn Reson Imaging Clin N Am* 1999;7(2):237–54, vii – viii.
  30. Griswold MA., Jakob PM., Heidemann RM., et al. Generalized Autocalibrating Partially Parallel Acquisitions (GRAPPA). *Magn Reson Med* 2002;47(6):1202–10. Doi: 10.1002/mrm.10171.
  31. Lustig, Michael and Donoho, David L and Santos, Juan M and Pauly JM. Compressed sensing MRI. *Signal Process Mag IEEE* 2008;25(2):72–82. Doi: Doi 10.1109/Tit.2006.871582.

32. Lustig M., Pauly JM. SPIRiT: Iterative self-consistent parallel imaging reconstruction from arbitrary k-space. *Magn Reson Med* 2010;64(2):457–71. Doi: 10.1002/mrm.22428.
33. Feinberg DA., Setsompop K. Ultra-fast MRI of the human brain with simultaneous multi-slice imaging. *J Magn Reson* 2013;229:90–100. Doi: 10.1016/j.jmr.2013.02.002.
34. Radiology M. Clinical Cardiac MRI. *Radiology* 2006;241(3):686–7. Doi: 10.1148/radiol.2413062590.
35. Nocedal J., Wright SJ. *Numerical Optimization*. vol. 43. 1999.
36. Schülen V., Schick F., Loichat J., et al. Evaluation of K-space segmented cine sequences for fast functional cardiac imaging. *Invest Radiol* 1996;31(8):512–22. Doi: 10.1097/00004424-199608000-00007.
37. Suga M., Matsuda T., Komori M., Minato K., Takahashi T. Keyhole method for high-speed human cardiac cine MR imaging. *J Magn Reson Imaging* 1999;10(5):778–83. Doi: 10.1002/(SICI)1522-2586(199911)10:5<778::AID-JMRI23>3.0.CO;2-2.
38. Tsao J., Boesiger P., Pruessmann KP. k-t BLAST and k-t SENSE: Dynamic MRI With High Frame Rate Exploiting Spatiotemporal Correlations. *Magn Reson Med* 2003;50(5):1031–42. Doi: 10.1002/mrm.10611.
39. Madore B., Glover GH., Pelc NJ. Unaliasing by Fourier-encoding the overlaps using the temporal dimension (UNFOLD), applied to cardiac imaging and fMRI. *Magn Reson Med* 1999;42(5):813–28. Doi: 10.1002/(SICI)1522-2594(199911)42:5<813::AID-MRM1>3.0.CO;2-S.
40. Gamper U., Boesiger P., Kozerke S. Compressed sensing in dynamic MRI. *Magn Reson Med* 2008;59(2):365–73. Doi: 10.1002/mrm.21477.
41. Montesinos P., Abascal JFPJ., Cussó L., Vaquero JJ., Desco M. Application of the compressed sensing technique to self-gated cardiac cine sequences in small animals. *Magn Reson Med* 2014;72(2):369–80. Doi: 10.1002/mrm.24936.
42. Pruessmann KP. Encoding and reconstruction in parallel MRI. *NMR Biomed* 2006;19(3):288–99. Doi: 10.1002/nbm.1042.
43. Brummer ME., Moratal-Pérez D., Hong CY., Pettigrew RI., Millet-Roig J., Dixon WT. Noquist: Reduced Field-of-View Imaging by Direct Fourier Inversion. *Magn Reson Med* 2004;51(2):331–42. Doi: 10.1002/mrm.10694.
44. Hamilton LH., Fabregat JA., Moratal D., et al. “pINOT”: Time-resolved parallel magnetic resonance imaging with a reduced dynamic field of view. *Magn Reson Med* 2011;65(4):1062–75. Doi: 10.1002/mrm.22696.
45. Feinberg DA., Hoenninger JC., Crooks LE., et al. Inner volume MR imaging: technical concepts and their application. *Radiology* 1985;156(3):743–7. Doi: 10.1148/radiology.156.3.4023236.
46. Vincenti G., Monney P., Chaptinel J., et al. Compressed Sensing Single-Breath-Hold CMR for Fast Quantification of LV Function, Volumes, and Mass. *JACC Cardiovasc Imaging* 2014;7(9):882–92. Doi: 10.1016/j.jcmg.2014.04.016.
47. World Health Organization (WHO). *Global Status Report on Non-Communicable*

- Diseases. Global Status Report on Non-Communicable Diseases. Available at: [http://www.who.int/nmh/publications/ncd\\_report\\_full\\_en.pdf](http://www.who.int/nmh/publications/ncd_report_full_en.pdf).
48. Nichols M., Townsend N., Scarborough P., Rayner M. European Cardiovascular Disease Statistics 2012. 2012.
  49. Gatehouse PD., Elkington AG., Ablitt N a., Yang G-Z., Pennell DJ., Firmin DN. Accurate assessment of the arterial input function during high-dose myocardial perfusion cardiovascular magnetic resonance. *J Magn Reson Imaging* 2004;20(1):39–45. Doi: 10.1002/jmri.20054.
  50. Ishida M., Schuster A., Morton G., et al. Development of a universal dual-bolus injection scheme for the quantitative assessment of myocardial perfusion cardiovascular magnetic resonance. *J Cardiovasc Magn Reson* 2011;13(1):28. Doi: 10.1186/1532-429X-13-28.
  51. Sánchez-González J., Fernandez-Jiménez R., Nothnagel ND., López-Martín G., Fuster V., Ibañez B. Optimization of dual-saturation single bolus acquisition for quantitative cardiac perfusion and myocardial blood flow maps. *J Cardiovasc Magn Reson* 2015;17(1):21. Doi: 10.1186/s12968-015-0116-2.
  52. Goodwill PW., Saritas EU., Croft LR., et al. X-Space MPI: Magnetic nanoparticles for safe medical imaging. *Adv Mater* 2012;24(28):3870–7. Doi: 10.1002/adma.201200221.
  53. Gleich B., Weizenecker J., Timminger H., et al. Fast MPI Demonstrator with Enlarged Field of View. *Proceedings of ISMRM*. 2010.
  54. Rahmer J., Gleich B., Bontus C., et al. Results on Rapid 3D Magnetic Particle Imaging with a Large Field of View. *ISMRM, 19th Annual Meeting, International Society for Magnetic Resonance in Medicine*. 2011. p. 19:629.
  55. Rahmer J., Weizenecker J., Gleich B., Borgert J. Signal encoding in magnetic particle imaging: properties of the system function. *BMC Med Imaging* 2009;9:4. Doi: 10.1186/1471-2342-9-4.
  56. Halkola A., Buzug TM., Rahmer J., Gleich B., Bontus C. System Calibration Unit for Magnetic Particle Imaging: Focus Field Based System Function. *Springer Proc Phys* 2012;140:27.
  57. Knopp T., Sattel TF., Biederer S., et al. Model-based reconstruction for magnetic particle imaging. *IEEE Trans Med Imaging* 2010;29(1):12–8. Doi: 10.1109/TMI.2009.2021612.
  58. Knopp T., Weber A. Sparse reconstruction of the magnetic particle imaging system matrix. *IEEE Trans Med Imaging* 2013;32(8):1473–80. Doi: 10.1109/TMI.2013.2258029.
  59. Gruettner M., Graeser M., Biederer S., et al. 1D-image reconstruction for magnetic particle imaging using a hybrid system function. *2011 IEEE Nucl Sci Symp Conf Rec* 2011:2545–8. Doi: 10.1109/NSSMIC.2011.6152687.
  60. Wawrzik T., Kuhlmann C., Ludwig F., Schilling M. Scanner setup and reconstruction for magnetic particle imaging. *Proc. SPIE*. 2013. p. 8672.
  61. Rahmer J., Weizenecker J., Gleich B., Borgert J. Analysis of a 3-D system function measured for magnetic particle imaging. *IEEE Trans Med Imaging* 2012;31(6):1289–99. Doi: 10.1109/TMI.2012.2188639.

62. Hansen P. Rank-deficient and discrete ill-posed problems: numerical aspects of linear inversion. 1998.
63. Kozerke S., Tsao J., Razavi R., Boesiger P. Accelerating cardiac cine 3D imaging using k-t BLAST. *Magn Reson Med* 2004;52(1):19–26. Doi: 10.1002/mrm.20145.
64. Niendorf T., Bunke J., Kouwenhoven M., et al. Single Breath-Hold Whole-Heart 3D CINE Imaging Using kt-BLAST and kt-SENSE. Proceedings 14th Scientific Meeting, International Society for Magnetic Resonance in Medicine. 2006. p. 1634.
65. Huber S., Muthupillai R., Mojibian H., Cheong B., Kouwenhoven M., Flamm SD. Rapid assessment of regional and global left ventricular function using three-dimensional k-t BLAST imaging. *Magn Reson Imaging* 2008;26(6):727–38. Doi: 10.1016/j.mri.2008.01.027.
66. Okuda S., Yamada Y., Tanimoto A., et al. Three-dimensional cardiac cine imaging using the kat ARC acceleration: Initial experience in clinical adult patients at 3T. *Magn Reson Imaging* 2015;33(7). Doi: 10.1016/j.mri.2015.04.004.
67. Jeong D., Schiebler ML., Lai P., Wang K., Vigen KK., François CJ. Single breath hold 3D cardiac cine MRI using kat-ARC: preliminary results at 1.5T. *Int J Cardiovasc Imaging* 2015. Doi: 10.1007/s10554-015-0615-0.
68. Hong J., Jaeheung Y., Jong CY. Generalized K-T blast and K-T sense using focuss. 2007 4th IEEE International Symposium on Biomedical Imaging: From Nano to Macro - Proceedings. 2007. p. 145–8.
69. Madore B. UNFOLD-SENSE: A parallel MRI method with self-calibration and artifact suppression. *Magn Reson Med* 2004;52(2):310–20. Doi: 10.1002/mrm.20133.
70. Van Den Brink JS., Watanabe Y., Kuhl CK., et al. Implications of SENSE MR in routine clinical practice. *Eur J Radiol* 2003;3–27. Doi: 10.1016/S0720-048X(02)00333-9.
71. Foo TK., Aisen AM., Hernandez RJ., Collick BD., Bernstein T., Bernstein MA. Improved ejection fraction and flow velocity estimates with use of view sharing and uniform repetition time excitation with fast cardiac techniques. *Radiology* 1995;195(2):471–8. Doi: 10.1148/radiology.195.2.7724769.
72. Makowski MR., Wiethoff AJ., Jansen CH., et al. Single breath-hold assessment of cardiac function using an accelerated 3D single breath-hold acquisition technique - comparison of an intravascular and extravascular contrast agent. *J Cardiovasc Magn Reson* 2012;14(1):53. Doi: 10.1186/1532-429X-14-53.
73. Fuderer M., van den Brink J., Jurrissen M. SENSE reconstruction using feed forward regularization. ISMRM, 11th Annual Meeting, International Society for Magnetic Resonance in Medicine, Abstract 2130. 2004.
74. Sch??r M., Kozerke S., Fischer SE., Boesiger P. Cardiac SSFP Imaging at 3 Tesla. *Magn Reson Med* 2004;51(4):799–806. Doi: 10.1002/mrm.20024.
75. Mueller A., Kouwenhoven M., Naehle CP., et al. Dual-Source Radiofrequency Transmission with Patient-Adaptive Local Radiofrequency Shimming for 3.0-T Cardiac MR Imaging: Initial Experience. *Radiology* 2012:77–85. Doi: 10.1148/radiol.11110347.
76. Weiger M., Pruessmann KP., Leussler C., Röschmann P., Boesiger P. Specific coil design

- for sense: A six-element cardiac array. *Magn Reson Med* 2001;45(3):495–504. Doi: 10.1002/1522-2594(200103)45:3<495::AID-MRM1065>3.0.CO;2-V.
77. Wech T., Pickl W., Tran-Gia J., et al. Whole-heart cine MRI in a single breath-hold - A compressed sensing accelerated 3D acquisition technique for assessment of cardiac function. *RoFo Fortschritte Auf Dem Gebiet Der Rontgenstrahlen Und Der Bildgeb Verfahren* 2014;186(1):37–41. Doi: 10.1055/s-0033-1350521.
  78. Lai P., Vasanawala S., Nozaki A., Funkg M., Brau A. Improving k-t autocalibrating parallel imaging for 3D cardiac cine MRI using priorreconstruction static tissue estimation and elimination. ISMRM, 21st Annual Meeting, International Society for Magnetic Resonance in Medicine, Abstract 0128. 2013.
  79. Borlaug B., Paulus W. Heart failure with preserved ejection fraction: pathophysiology, diagnosis, and treatment. *Eur Hear J* 2011;32:670–9. Doi: 10.1093/eurheartj/ehq426.
  80. Curtis JP., Sokol SI., Wang Y., et al. The association of left ventricular ejection fraction, mortality, and cause of death in stable outpatients with heart failure. *J Am Coll Cardiol* 2003;42(4):736–42. Doi: 10.1016/S0735-1097(03)00789-7.
  81. Kramer CM., Barkhausen J., Flamm SD., Kim RJ., Nagel E. Standardized cardiovascular magnetic resonance imaging (CMR) protocols, society for cardiovascular magnetic resonance: board of trustees task force on standardized protocols. *J Cardiovasc Magn Reson* 2008;10(1):35. Doi: 10.1186/1532-429X-10-35.
  82. Xue H., Kellman P., LaRocca G., Arai AE., Hansen MS. High spatial and temporal resolution retrospective cine cardiovascular magnetic resonance from shortened free breathing real-time acquisitions. *J Cardiovasc Magn Reson* 2013;15(1):102. Doi: 10.1186/1532-429X-15-102.
  83. Nothnagel N., Fernandez-Jiménez R., Kouwenhoven M., et al. VF 3D-BRISA: Very Fast 3D BREath-hold Isotropic imaging using Spatio-temporal Acceleration for non-angulated whole-chest cardiac cine MRI. *Magn Reson Med* 2016.
  84. Fernández-Jiménez R., Sánchez-González J., Agüero J., et al. Myocardial Edema After Ischemia/Reperfusion Is Not Stable and Follows a Bimodal Pattern. *J Am Coll Cardiol* 2015;65(4):315–23. Doi: 10.1016/j.jacc.2014.11.004.
  85. Nothnagel N., Fernandez-Jiménez R., López-Martín G., Desco M., Fuster V., Ibañez B. CASI-SENSE: A novel reconstruction strategy for 3D single breath-hold isotropic cine imaging Background. ISMRM, 23rd Annual Meeting: Toronto Canada. International Society for Magnetic Resonance in Medicine. 2015. p. 3131.
  86. Passing H., Bablok W. A new biometrical procedure for testing the equality of measurement from two different analytical methods. Application of linear regression procedures for method comparison studies in Clinical Chemistry, Part 1. *J Clin Chem Clin Biochem* 1983;21(11):709–20. Doi: 10.1515/cclm.1983.21.11.709.
  87. Bland JM., Altman DG. Statistical methods for assessing agreement between two methods of clinical measurement. *Lancet* 1986;1(8476):307–10. Doi: 10.1016/S0140-6736(86)90837-8.
  88. Kirschbaum SW., Baks T., Gronenschild EH., et al. Addition of the long-axis information to short-axis contours reduces interstudy variability of left-ventricular analysis in cardiac magnetic resonance studies. *Invest Radiol* 2008;43(1):1–6. Doi:

10.1097/RLI.0b013e318154b1dc.

89. Pruessmann KP., Weiger M., Börnert P., Boesiger P. Advances in sensitivity encoding with arbitrary k-space trajectories. *Magn Reson Med* 2001;46(4):638–51. Doi: 10.1002/mrm.1241.
90. Selvanayagam JB., Kardos A., Francis JM., et al. Value of delayed-enhancement cardiovascular magnetic resonance imaging in predicting myocardial viability after surgical revascularization. *Circulation* 2004;110(12):1535–41. Doi: 10.1161/01.CIR.0000142045.22628.74.
91. Hsu LY., Rhoads KL., Holly JE., Kellman P., Aletras AH., Arai AE. Quantitative myocardial perfusion analysis with a dual-bolus contrast-enhanced first-pass MRI technique in humans. *J Magn Reson Imaging* 2006;23(3):315–22. Doi: 10.1002/jmri.20502.
92. Ichihara T., Ishida M., Kitagawa K., et al. Quantitative analysis of first-pass contrast-enhanced myocardial perfusion MRI using a Patlak plot method and blood saturation correction. *Magn Reson Med* 2009;62(2):373–83. Doi: 10.1002/mrm.22018.
93. Johnson R., Noble N., Muthurangu V., et al. 32-Channel Non-Angulated Cine Cardiac Volumes - Automatic Reformatting. *Proceedings 14th Scientific Meeting, International Society for Magnetic Resonance in Medicine*. 2006. p. 791.
94. Moratal D., Thomas Dixon W., Ramamurthy S., Lerakis S., James Parks W., Brummer ME. Optimal sampling for “Noquist” reduced-data cine magnetic resonance imaging. *Med Phys* 2013;40(1):12302. Doi: 10.1118/1.4770270.